Extremal inclusions in nonlinear conductivity

Michaël Peigney

Extremal inclusions in nonlinear conductivity

Michaël Peigney

Lab Navier, Univ Gustave Eiffel, ENPC, CNRS, F-77447 Marne la Vallée, France

Abstract

We consider two-phase composites whose microstructures are two-dimensional and generated by the periodic replication of a convex polygonal cell containing a single inclusion embedded in a matrix. Adopting the framework of nonlinear conductivity, we address the problem of finding the inclusion shape that optimizes the effective energy. A conceptually simple but numerically effective approach is presented, in which the inclusion shape is parameterized by the Fourier coefficients of a scalar periodic function f that defines its polar representation. Truncating the Fourier expansion to a finite order turns the shape optimization problem into a finite-dimensional constrained optimization problem that can be solved using a numerical algorithm of choice. Explicit expressions of the function to optimize and its gradient are provided and can easily be evaluated from a finite-element model. The proposed approach is applied to perfectly conducting inclusions in a power law matrix. Results for the three types of regular tessellations (square, hexagonal and triangular) are presented and compared with the Vigdergauz (1994, 1999) microstructures giving the extremal inclusions in the linear case. The proposed method gives very simple representations of the extremal inclusions, which could useful for manufacturing the microstructures considered. The obtained nonlinear effective conductivities are compared with known

Email address: michael.peigney@polytechnique.org (Michaël Peigney)

Hashin-Shtrikman type nonlinear bounds, which contributes to shed some light on the optimality of those bounds.

Keywords: inclusion problem, periodic homogenization, shape optimization, nonlinear conductivity, bounds

---

1. Introduction

Consider a two-phase composite conductor in which the constitutive materials are isotropic with given energy density functions. The effective energy function of the composite depends on the microstructure, i.e. on the geometrical arrangement of the phases. For linear conductors with statistically isotropic microstructures, Hashin and Shtrikman (1962) derived both upper and lower bounds on the effective energy. Those bounds are optimal in the sense that there exist some microstructures that saturate the bounds. Various examples of such extremal microstructures are known. The earliest one is the coated sphere assemblage of Hashin and Shtrikman (1962). An other possible construction is obtained by sequential lamination (Lurie and Cherkaev, 1984; Murat and Tartar, 1985). Both those types of microstructures are relatively difficult to manufacture, even in two dimensions. In that regard, simpler microstructures have been proposed by Vigdergauz (1994, 1999) by considering periodic arrangements of identical inclusions. Those microstructures are generated by the periodic replication of a regular polygonal cell made of an inclusion embedded in a matrix. Square tessellations were first considered in Vigdergauz (1994). Hexagonal and triangular tessellations were later considered in Vigdergauz (1999). For all those three types of tessellations, Vigdergauz (1994, 1999) showed that is is possible to choose the shape of the inclusion in such fashion that the effective energy of the

periodic microstructure coincide with the Hashin-Shtrikman bounds[1]. Vigdergauz (1994, 1999) used analytical techniques such as holomorphic functions and conformal mapping. The obtained expressions for the inclusion shapes are not explicit and relatively complex. For square tessellations, Grabovsky and Kohn (1995) obtained an explicit expression for the shape of the inclusion in terms of elliptic functions.

Numerical approaches have also been studied to find optimal inclusion in linear problems. Vigdergauz (2001) notably used a genetic algorithm for finding the inclusion shapes that maximize the effective shear moduli in a perforated elastic plate. The optimal shape was parameterized using a number M of control points on the boundary of the inclusion (with M in the range 60–90 depending on the tessellation). Later Vigdergauz (2010) used a genetic algorithm in combination with a truncated Laurent series for the conformal mapping of the unit circle to the inclusion shape, which reduced the number of parameters needed for describing the optimal inclusion to a good approximation (truncated series of order 7 were typically used). Topology optimization methods have also been used to generate Vidgergauz-like inclusions for square tessellations in linear elasticity (see e.g. the books by Allaire (2012); Bendsøe and Sigmund (2013) for a detailed introduction to topology optimization).

This paper aims at pushing the constructions of Vigdergauz (1994, 1999) to nonlinear conductivity. In more detail, we consider the shape optimization problem of finding the inclusion shape that optimizes the effective energy of a periodic two-phase

[1]It should be noted that Vigdergauz (1994, 1999) dealt with elasticity problems rather than conductivity problems, more specifically considering the problem of finding microstructures of extremal bulk modulus. Those microstructures can be shown to be also extremal for the conductivity problem. This results from the cross-properties of Gibiansky and Torquato (1995), as detailed in Appendix B

composite when the constitutive materials are nonlinear and the volume fractions are prescribed. As detailed in Sect. 2, we parameterize the shape of the inclusion using a scalar $2\pi-$periodic function f that gives the polar representation of the boundary of the inclusion. Imposing the volume fractions sets an integral constraint on f. In mathematical terms, the problem to be solved becomes a constrained optimization problem in the functional space of 2π-periodic functions. Local optimality conditions are derived in Sect. 3 using techniques from calculus of variations. In the nonlinear case there is little hope to obtain exact solutions using analytical techniques so we resort to approximation methods instead. In Sect. 4 is proposed a relatively simple method for constructing approximate solutions in the general case. That method is based on the idea of approximating $2\pi-$periodic function f by considering finite partial sums of Fourier series. The optimization is thus restricted to a finite-dimensional set of functions that satisfy the required constraints, in the spirit of Galerkin methods. In practice that finite-dimensional optimization problem can be solved by combining finite-element techniques and a descent algorithm. The gradient of the function to be optimized is obtained from the results of Sect. 3 and can easily be evaluated from finite-element simulations.

The proposed method has been applied to composites made of perfectly conducting inclusions in a power law matrix. Results from square, hexagonal and triangular tessellations are presented in Sects. 5, 6 and 7, respectively. In the linear case, the microstructures of Vigdergauz (1994, 1999) are recovered. The influence of the nonlinearity on the obtained inclusions is discussed in detail. The proposed method gives very simple representations of the extremal inclusions, with very few parameters (3 to 7, depending on the tessellation), which could useful for manufacturing the microstructures considered. The effective conductivities of the optimized microstructures are compared with relevant bounds from the literature, most notably

the Hashin-Shtrikman type bounds of Talbot and Willis (1985); Ponte Castañeda et al. (1992); Peigney and Peigney (2017). This allows one to get some partial information on the optimality of those bounds. Concluding remarks follow in Sect. 8.

2. Formulation of the problem

We consider the class of two-dimensional microstructures that are generated by regular tessellations of convex polygonal cells where all the cells are identical and consist of a single inclusion of material 1 embedded in a material 2. It is known that there exists only three regular tessellations, corresponding to square, triangular and hexagonal cells as represented in Fig. 1 (Singer, 1998). Those three tessellations differ by the order n of rotational symmetry of the basic cell Ω: n is equal to 3 for triangular tessellations, 4 for square tessellations and 6 for hexagonal tessellations. We require the inclusion to have the same $n-$fold rotational symmetry as the basic cell, which is a sufficient (but not necessary) condition for the effective behavior to have $n-$fold symmetry. In such case, rigorous bounds on the effective properties are available as will be detailed later on.

We are interested in finding the inclusion shape that optimizes the effective energy for prescribed volume fractions of materials 1 and 2. Let us formulate the problem in more detail, focusing first on square and hexagonal tessellations. In those cases, the tessellation is periodic and the periodic cell can be chosen as equal to Ω. The effective energy w_{eff} is given by

$$w_{\mathit{eff}}(\bar{\boldsymbol{e}}) = \inf_{u \text{ periodic}} \frac{1}{|\Omega|} \int_\Omega \sum_{i=1}^{2} \chi_i(\boldsymbol{x}) w_i(\bar{\boldsymbol{e}} + \nabla u) d\omega \tag{1}$$

where w_i is the energy density function of material i and χ_i is the characteristic function of the domain Ω_i occupied by material i ($\chi_i(\boldsymbol{x}) = 1$ if $\boldsymbol{x} \in \Omega_i$, $\chi_i(\boldsymbol{x}) = 0$

otherwise). Determining $w_{\mathit{eff}}(\bar{\boldsymbol{e}})$ formally amounts to solve the local equations

$$\operatorname{div} \boldsymbol{j} = 0,\ \boldsymbol{j} = \sum_{i=1}^{2} \chi_i(\boldsymbol{x}) w_i'(\bar{\boldsymbol{e}} + \nabla u),\ u \text{ periodic, } \boldsymbol{j} \cdot \boldsymbol{n} \text{ anti-periodic.} \tag{2}$$

Adopting the terminology of electrical conductivity, the field $\boldsymbol{j}$ in (2) is the current density and and $\boldsymbol{e} = \bar{\boldsymbol{e}} + \nabla u$ is the electric field. In (1), $\bar{\boldsymbol{e}}$ is the effective (or average) electric field. One could alternatively consider thermal conductivity, magnetic permeability or diffusion as all those problems are governed by the same equations. The elasticity problem of torsion in a cylinder also falls under the umbrella of the framework considered.

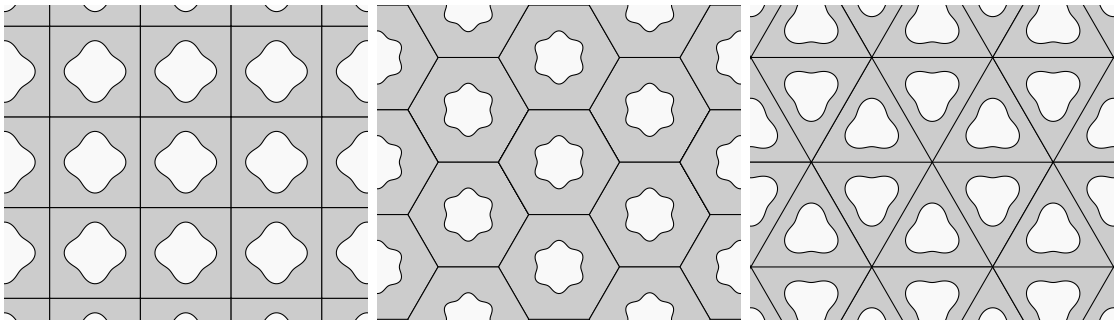

Figure 1: The three classes of regular tessellations as considered in the paper (from left to right: square, hexagonal, triangular). The basic cell contains a single inclusion that has the same order of rotational symmetry as the cell itself.

If the energy density functions w_i $(i = 1, 2)$ are known and $\bar{\boldsymbol{e}}$ is prescribed, then $w_{\mathit{eff}}(\bar{\boldsymbol{e}})$ can be viewed as a function of the domain Ω_1. We denote by $J(\Omega_1)$ the effective energy corresponding to a given inclusion shape Ω_1, i.e.

$$J(\Omega_1) = \frac{1}{|\Omega|} \int_{\Omega} \sum_{i=1}^{2} \chi_i(\boldsymbol{x}) w_i(\bar{\boldsymbol{e}} + \nabla u) d\omega \tag{3}$$

where u attains the minimum in (1). We consider the problem of optimizing J with respect to domains Ω_1 such that

(i) Ω_1 has $n-$fold rotational symmetry

(ii) The volume fraction $|\Omega_1|/|\Omega|$ is prescribed

(iii) Ω_1 is a star-shaped set around the center O of the cell Ω.

Requirement (iii) is a sufficient (but not necessary) condition for the domain Ω_1 to be of the inclusion type, i.e. to be a simply, connected set. The motivation for introducing requirement (iii) is that it makes for a simple representation of the geometry Ω_1. Using coordinates centered at O, any domain fulfilling (iii) can indeed be written as

$$\Omega_1(f) = \{\boldsymbol{x} = r\cos\theta\,\boldsymbol{u}_x + r\sin\theta\,\boldsymbol{u}_y : 0 \leq r \leq f(\theta)\} \tag{4}$$

where $f : \mathbb{R} \mapsto \mathbb{R}$ is a $2\pi-$periodic function (Fig. 2). Note that requirement (i) implies that f is actually $\frac{2\pi}{n}-$periodic. Denoting by c_1 the volume fraction of material 1, requirement (ii) translates as

$$c_1|\Omega| = \int_0^{2\pi} \frac{1}{2} f^2(\theta) d\theta. \tag{5}$$

We focus on minimizing J in the rest of the paper (the issue of maximizing J could be handled similarly). The problem to be solved becomes

$$\min_{f \in \mathcal{K}(c_1)} J(\Omega_1(f)) \tag{6}$$

where

$$\mathcal{K}(c_1) = \left\{ f : f\ \tfrac{2\pi}{n}\text{-periodic},\ \int_0^{2\pi} \frac{1}{2} f^2(\theta) d\theta = c_1|\Omega| \right\}. \tag{7}$$

As common in shape optimization problems, the difficulty in solving (6) lies in the fact that the function J is not expressed explicitly in terms of f: For a given f, evaluating $J(\Omega_1(f))$ requires solving the nonlinear boundary value problem (2) which is parametrized by f. In the next Section, we derive the expression of the gradient of J with respect to f and study optimality conditions in problem (6).

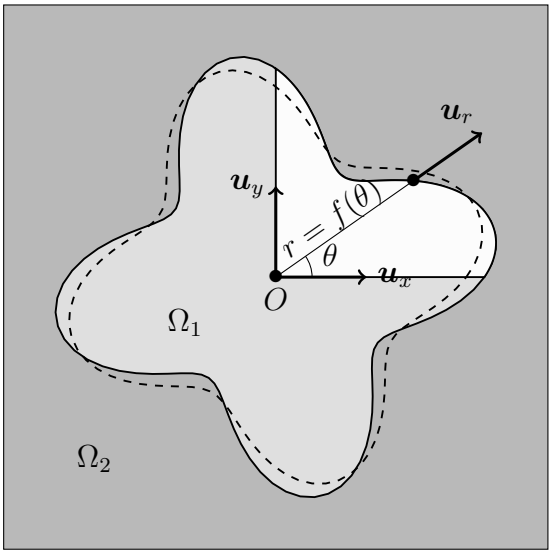

Figure 2: Parameterization for the shape of the inclusion in a square periodic cell. The inclusion is required to have 4−fold symmetry so that degrees of freedom correspond to one quarter (shown in white) of the inclusion. The dashed line represents the boundary of the inclusion for a variation $\partial\Omega_1$.

3. Optimality conditions

Let Ω_1 be a given arbitrary inclusion (not necessarily star-shaped or n-fold symmetric). Considering a variation $\delta\Omega_1$ of the shape of the inclusion, we calculate the corresponding variation δJ of the functional J in (3). A variation $\delta\Omega_1$ can be represented by a infinitesimal displacement $\delta\boldsymbol{\xi}(\boldsymbol{x})$ of the boundary $\partial\Omega_1$. The corresponding variation δJ is

$$\delta J = \frac{1}{|\Omega|}\int_{\partial\Omega_1} [\![w]\!](\delta\boldsymbol{\xi}\cdot\boldsymbol{n})ds + \frac{1}{|\Omega|}\int_{\Omega}\sum_{i=1}^{2}\chi_i(\boldsymbol{x})w_i'(\bar{\boldsymbol{e}}+\nabla u)\cdot(\nabla\delta u)d\omega \qquad (8)$$

where $[\![w]\!] = w_2(\bar{\boldsymbol{e}}+\nabla u) - w_1(\bar{\boldsymbol{e}}+\nabla u)$, $\boldsymbol{n}$ is the normal to Ω_1 and δu is the variation of the solution to (1). Since u satisfies (2), the second integral on the right hand of

(8) vanishes[2]. Thus we have

$$\delta J = \frac{1}{|\Omega|} \int_{\partial\Omega_1} [\![w]\!](\delta\boldsymbol{\xi} \cdot \boldsymbol{n}) ds. \tag{9}$$

Expressing the volume $|\Omega_1|$ of the inclusion as the integral $|\Omega_1| = \int_\Omega \chi_1(\boldsymbol{x}) dx$, we obtain in a similar fashion that the variation $\delta|\Omega_1|$ of the volume of the inclusion is given by

$$\delta|\Omega_1| = \int_{\partial\Omega_1} (\delta\boldsymbol{\xi} \cdot \boldsymbol{n}) ds. \tag{10}$$

Let $\partial\Omega_1^k$ be the intersection of $\partial\Omega_1$ with the angular sector $2\pi k/n \leq \theta \leq 2\pi(k+1)/n$ where n is the order of rotational symmetry of the basic cell Ω. Eq. (10) can be rewritten as

$$\delta|\Omega_1| = \sum_{k=0}^{n-1} \int_{\partial\Omega_1^k} (\delta\boldsymbol{\xi} \cdot \boldsymbol{n}) ds. \tag{11}$$

Eqs. (9), (10) and (11) hold for any domain Ω_1 and variation $\delta\Omega_1$. We now specialize those relations to the case where both Ω_1 and $\delta\Omega_1$ have $n-$fold symmetry. In that case, all the n integrals on the right hand side of (11) take the same value so that

$$\delta|\Omega_1| = n \int_{\partial\Omega_1^0} (\delta\boldsymbol{\xi} \cdot \boldsymbol{n}) ds. \tag{12}$$

Expression (9) can be rewritten similarly as

$$\delta J = \frac{1}{|\Omega|} \sum_{k=0}^{n-1} \int_{\partial\Omega_1^k} [\![w]\!](\delta\boldsymbol{\xi} \cdot \boldsymbol{n}) ds \tag{13}$$

In contrast with (12), there is no reason for the integrals on the right-hand side of (13) to be equal because the solution u to (1) – and consequently the term $[\![w]\!]$ in (13) –

[2]Using (2), that integral can be indeed be rewritten as $\frac{1}{|\Omega|}\int_\Omega \boldsymbol{j} \cdot (\nabla\delta u) d\omega$ and we have $\int_\Omega \boldsymbol{j} \cdot (\nabla\delta u) d\omega = -\int_\Omega \delta u \operatorname{div} \boldsymbol{j} d\omega + \int_{\partial\Omega} (\boldsymbol{j} \cdot \boldsymbol{n}) \delta u ds$. Now $\operatorname{div} \boldsymbol{j} = 0$ from (2) and $\int_{\partial\Omega} (\boldsymbol{j} \cdot \boldsymbol{n}) \delta u ds = 0$ because δu is periodic and $\boldsymbol{j} \cdot \boldsymbol{n}$ is anti-periodic.

depend on the loading $\bar{\boldsymbol{e}}$ and are not expected to have $n-$fold rotational symmetry. In order to reduce δJ to an integral over $\partial\Omega_1^0$, it is convenient to introduce the operator $\cdot_{sym}$ that maps any given field v to the $n-$fold symmetric field v_{sym} defined by

$$v_{sym}(\boldsymbol{x}) = \frac{1}{n}\sum_{k=0}^{n-1} v(\boldsymbol{R}_k \cdot \boldsymbol{x})$$

where $\boldsymbol{R}_k$ is the rotation with center O and angle $2\pi k/n$. Using the change of variable $\boldsymbol{x} = \boldsymbol{R}_k \cdot \boldsymbol{y}$ and recalling that Ω_1 and $\delta\boldsymbol{\xi}$ have $n-$fold symmetry, we have

$$\int_{\partial\Omega_1^k} [\![w]\!](\boldsymbol{x})(\delta\boldsymbol{\xi}(\boldsymbol{x})\cdot\boldsymbol{n}(\boldsymbol{x}))ds = \int_{\partial\Omega_1^0} [\![w]\!](\boldsymbol{R}_k\cdot\boldsymbol{y})(\delta\boldsymbol{\xi}(\boldsymbol{y})\cdot\boldsymbol{n}(\boldsymbol{y}))ds$$

hence

$$\delta J = \frac{1}{|\Omega|}\int_{\partial\Omega_1^0}\left(\sum_{k=0}^{n-1}[\![w]\!](\boldsymbol{R}_k\cdot\boldsymbol{y})\right)(\delta\boldsymbol{\xi}(\boldsymbol{y})\cdot\boldsymbol{n}(\boldsymbol{y}))ds$$

i.e.

$$\delta J = \frac{n}{|\Omega|}\int_{\partial\Omega_1^0}[\![w]\!]_{sym}(\delta\boldsymbol{\xi}\cdot\boldsymbol{n})ds. \tag{14}$$

Consider an inclusion shape Ω_1 that minimizes J with respect to *all* $n-$fold symmetric inclusions of given volume. From (12) and (14), the first order optimality condition reads as

$$\int_{\partial\Omega_1^0}[\![w]\!]_{sym}(\delta\boldsymbol{\xi}\cdot\boldsymbol{n})ds = 0 \tag{15}$$

for any $n-$fold symmetric displacement $\delta\boldsymbol{\xi}$ such that $\int_{\partial\Omega_1^0}\delta\boldsymbol{\xi}\cdot\boldsymbol{n}\,ds = 0$. Condition (15) can be seen to impose that

$$[\![w]\!]_{sym} \textit{ constant on } \partial\Omega_1. \tag{16}$$

Let indeed $\boldsymbol{x}_0$ and $\boldsymbol{x}_1$ be two given distinct points on $\partial\Omega_1^0$ and consider the $n-$fold symmetric displacement

$$\boldsymbol{\xi}^* = \eta(\delta_{\boldsymbol{x}_0}\boldsymbol{n}(\boldsymbol{x}_0) - \delta_{\boldsymbol{x}_1}\boldsymbol{n}(\boldsymbol{x}_1))_{sym}$$

where $\eta > 0$ is an infinitesimally small parameter, $\delta_{\boldsymbol{x}_i}$ is the Dirac distribution defined on $\partial\Omega_1^0$ and concentrated at $\boldsymbol{x}_i$, and $\boldsymbol{n}(\boldsymbol{x}_i)$ is the normal to $\partial\Omega_1$ at $\boldsymbol{x}_i$. Since $\int_{\partial\Omega_1^0} \boldsymbol{\xi}^* \cdot \boldsymbol{n} ds = 0$, Eq. (15) implies that $\frac{n}{\eta} \int_{\partial\Omega_1^0} [\![w]\!]_{sym} \boldsymbol{\xi}^* \cdot \boldsymbol{n}\, ds = [\![w]\!]_{sym}(\boldsymbol{x}_0) - [\![w]\!]_{sym}(\boldsymbol{x}_1) = 0$, hence $[\![w]\!]_{sym}(\boldsymbol{x}_0) = [\![w]\!]_{sym}(\boldsymbol{x}_1)$. Property (16) follows.

Consider now problem (6) in which the optimization of J is restricted to domains $\Omega_1(f)$ that admit a representation of the form (4). Any point $\boldsymbol{x}$ on the boundary $\partial\Omega_1(f)$ can written as $\boldsymbol{x} = f(\theta)\boldsymbol{u}_r$ for some $\theta \in [0, 2\pi]$, where $\boldsymbol{u}_r$ is the unit radial vector (Fig. 2). In accordance with (4), variations $\delta\Omega_1$ are restricted to displacements $\delta\boldsymbol{\xi}$ of the form

$$\delta\boldsymbol{\xi} = \delta f(\theta)\boldsymbol{u}_r \tag{17}$$

where δf is a $2\pi/n-$periodic function. Further noting that $ds = \sqrt{(f')^2 + f^2}d\theta$ and $\boldsymbol{n} = (f\boldsymbol{u}_r - f'\boldsymbol{u}_\theta)/(\sqrt{(f')^2 + f^2})$, expressions (12) and (14) yield

$$\delta|\Omega_1| = n \int_0^{2\pi/n} \delta f(\theta) f(\theta) d\theta \tag{18}$$

$$\delta J = \frac{n}{|\Omega|} \int_0^{2\pi/n} [\![w]\!]_{sym} \delta f(\theta) f(\theta) d\theta. \tag{19}$$

The optimality condition now gives

$$\int_0^{2\pi/n} [\![w]\!]_{sym} \delta f(\theta) f(\theta) d\theta = 0$$

for any $2\pi/n-$periodic function δf such that $\int_0^{2\pi/n} \delta f(\theta) f(\theta) d\theta = 0$. Reproducing a similar argument as used earlier shows that the function f describing the optimal inclusion $\Omega_1(f)$ in (6) is such that (16) holds. Hence, if the inclusion $\Omega_1(f)$ is a local extremum of J with respect to all variation $\delta\Omega_1$ satisfying (17), then it is also a local extremum with respect to *any* $n-$ fold symmetric variation $\delta\Omega_1$ (not necessarily star-shaped).

4. Fourier expansion

We now describe an approximation method for solving problem (6). Any given function f in $\mathcal{K}(c_1)$ is $\frac{2\pi}{n}$-periodic and can thus be expanded as a Fourier series

$$f(\theta) = a_0 + \sum_{k=1}^{\infty} \{a_k \cos(kn\theta) + b_k \sin(kn\theta)\}. \tag{20}$$

The main idea of the proposed method is to approximate $\mathcal{K}(c_1)$ by considering partial sum of a given finite rank M in (20). In other words we approximate (6) by the finite dimensional minimization problem

$$\min_{f \in \mathcal{K}(c_1, M)} J(\Omega_1(f)) \tag{21}$$

where $\mathcal{K}(c_1, M) \subset \mathcal{K}(c_1)$ is the set constituted by functions of the form

$$f(\theta) = a_0 + \sum_{k=1}^{M} a_k \cos(kn\theta) + b_k \sin(kn\theta) \tag{22}$$

that satisfy the constraint (5). Parseval's identity shows that the function f in (22) verifies

$$\frac{1}{2\pi} \int_0^{2\pi} f^2(\theta) d\theta = a_0^2 + \frac{1}{2} \left(\sum_{k=1}^{M} a_k^2 + b_k^2 \right).$$

Hence the constraint (5) is satisfied provided that

$$c_1 \frac{|\Omega|}{\pi} = a_0^2 + \frac{1}{2} \left(\sum_{k=1}^{M} a_k^2 + b_k^2 \right). \tag{23}$$

We denote by $\mathcal{E}(c_1, M)$ the ellipsoid in $\mathbb{R}^{2M+1}$ that is defined by Eq. (23). Relation (22) defines a one-to-one mapping between functions f in $\mathcal{K}(c_1, M)$ and vectors $(a_0, \cdots, a_M, b_1, \cdots, b_M)$ in $\mathcal{E}(c_1, M)$. Identifying a function f in $\mathcal{K}(c_1, M)$ with the vector $\boldsymbol{X}$ formed by its Fourier coefficients $(a_0, \cdots, a_M, b_1, \cdots, b_M)$, problem (21) can be rewritten as

$$\min_{\boldsymbol{X} \in \mathcal{E}(c_1, M)} J(\Omega_1(\boldsymbol{X})). \tag{24}$$

The constrained optimization problem (24) is amenable to numerical techniques and can notably be solved using a projected gradient algorithm. The implementation of such an algorithm requires the expression of : (i) the gradient of J with respect to $\boldsymbol{X} = (a_0, \cdots, a_M, b_1, \cdots, b_M)$, (ii) the projection operator $\mathcal{P}$ on the set $\mathcal{E}(c_1, M)$. The expression of the gradient of J with respect to (a_k, b_k) follows from (19). Using the relation $\delta f = \delta a_0 + \sum_{k\geq 1} \delta a_k \cos(kn\theta) + \delta b_k \sin(kn\theta)$, we obtain

$$\frac{\partial J}{\partial a_k} = \frac{n}{|\Omega|}\int_0^{2\pi/n} [\![w]\!]_{sym} f(\theta)\cos nk\theta d\theta = \frac{1}{|\Omega|}\int_0^{2\pi} [\![w]\!] f(\theta)\cos nk\theta d\theta,$$

$$\frac{\partial J}{\partial b_k} = \frac{n}{|\Omega|}\int_0^{2\pi/n} [\![w]\!]_{sym} f(\theta)\sin nk\theta d\theta = \frac{1}{|\Omega|}\int_0^{2\pi} [\![w]\!] f(\theta)\sin nk\theta d\theta.$$

For any given $\boldsymbol{X}^0 \in \mathbb{R}^{2M+1}$, the projection $\mathcal{P}(\boldsymbol{X}^0)$ is defined by

$$\mathcal{P}(\boldsymbol{X}^0) = \underset{\boldsymbol{X}\in\mathcal{E}(c_1, M)}{\arg\min} \|\boldsymbol{X} - \boldsymbol{X}^0\|^2 \tag{25}$$

where $\|\cdot\|$ is the Euclidean norm. Even though $\mathcal{E}(c_1, M)$ is not convex, it can be shown that (25) admits a unique solution if $X_0^0 \neq 0$ (see Appendix A). Moreover, whatever M, it is shown in Appendix A that solving (25) reduces to solving a quartic equation on an interval $[\lambda_-(\boldsymbol{X}^0), \lambda_+(\boldsymbol{X}^0)]$ where λ_- and λ_+ are explicit functions of $\boldsymbol{X}^0$.

The shape optimization procedure for finding the inclusion of minimum energy is summarized in Algorithm 1 which is essentially a projected gradient algorithm with variable step size. The inputs are parameters $\boldsymbol{X}^0 = (a_0^0, \cdots, a_M^0, b_1^0, \cdots, b_M^0)$ defining a starting shape of the inclusion and an initial step size α_0. At each iteration, solving the boundary value problem (2) is needed for evaluating the function J in (3). This can be achieved using a finite element code. Note that extracting the values of $[\![w]\!]$ from the numerical solution of (2) allows one to evaluate the integrals $\int_0^{2\pi} [\![w]\!] f(\theta)\cos nk\theta d\theta$ and $\int_0^{2\pi} [\![w]\!] f(\theta)\sin nk\theta d\theta$ that define the descent direction in

the algorithm. The algorithm stops when either a maximum number N_{iter} of iterations is reached or the step size reaches a prescribed minimum value α_{min}. The output of Algorithm 1 are the parameters $\boldsymbol{X} = (a_0, \cdots, a_M, b_1, \cdots, b_M)$ defining the shape of the optimized inclusion. We note that the condition $f > 0$ of a positive radius is not enforced in the algorithm. In practice, Algorithm 1 was started from an initial inclusion shape satisfying $f > 0$ (a circular shape was often used) and the radius of the inclusion was found to remain strictly positive along the iterations.

Input : $\boldsymbol{X}^0 = (a_0^0, \cdots, a_M^0, b_1^0, \cdots, b_M^0)$, α_0

Output: $\boldsymbol{X} = (a_0, \cdots, a_M, b_1, \cdots, b_M)$

$\alpha \leftarrow \alpha_0$;

$\boldsymbol{X} \leftarrow \boldsymbol{X}^0$;

$N \leftarrow 1$;

repeat

  $u \leftarrow$ solution of (2) for $\Omega_1(\boldsymbol{X})$;

  $J \leftarrow \int_\Omega \sum_{i=1}^2 \chi_i(\boldsymbol{x}) w_i(\bar{\boldsymbol{e}} + \nabla u)$;

  $\boldsymbol{U} \leftarrow (\int_0^{2\pi} [\![w]\!] f(\theta) \cos nk\theta d\theta)_{0 \le k \le M}$;

  $\boldsymbol{V} \leftarrow (\int_0^{2\pi} [\![w]\!] f(\theta) \sin nk\theta d\theta)_{1 \le k \le M}$;

  $\boldsymbol{Y} \leftarrow (\boldsymbol{U}, \boldsymbol{V})$;

  repeat

    $\tilde{\boldsymbol{X}} \leftarrow \mathcal{P}(\boldsymbol{X} - \alpha \boldsymbol{Y})$;

    $\tilde{u} \leftarrow$ solution of (2) for $\Omega_1(\tilde{\boldsymbol{X}})$;

    $\tilde{J} \leftarrow \int_\Omega \sum_{i=1}^2 \chi_i(\boldsymbol{x}) w_i(\bar{\boldsymbol{e}} + \nabla \tilde{u})$;

    $\alpha \leftarrow \alpha/2$;

  until $\tilde{J} < J$;

  $\alpha \leftarrow 2\alpha$;

  $N \leftarrow N + 1$;

  $\boldsymbol{X} \leftarrow \tilde{\boldsymbol{X}}$;

until $\alpha < \alpha_{min}$ *or* $N > N_{iter}$;

Algorithm 1: Shape optimization algorithm.

5. Square tessellation

The proposed procedure has been applied to composites made of perfectly conducting inclusions in a power law matrix, i.e. the energy density functions w_1 and

w_2 are taken as

$$w_1(\boldsymbol{e}) = \begin{cases} 0 & \text{if } \boldsymbol{e} = 0 \\ +\infty & \text{otherwise} \end{cases} \tag{26}$$

$$w_2(\boldsymbol{e}) = \frac{\sigma_2}{m+1}|\boldsymbol{e}|^{m+1} \tag{27}$$

where m is the nonlinearity index and σ_2 is the conductivity parameter of the matrix. The energy density function in (26) is the limit case of a power law function $\frac{\sigma_1}{m+1}|\boldsymbol{e}|^{m+1}$ as the conductivity σ_1 becomes infinite. The composites considered here can thus be viewed as two-phase power law composites with an infinite contrast σ_1/σ_2. This is the most interesting situation where the effective properties show the largest variations with the microstructure. For the case considered, a standard argument of homogeneity shows that effective energy w_{eff} in (1) is positively homogeneous of degree $m+1$ and can thus be written as

$$w_{\mathit{eff}}(\bar{\boldsymbol{e}}) = \frac{\sigma_{\mathit{eff}}(\bar{\theta})}{m+1}|\bar{\boldsymbol{e}}|^{m+1} \tag{28}$$

where σ_{eff} is a function of the angle $\bar{\theta}$ between $\boldsymbol{u}_x$ and $\bar{\boldsymbol{e}}$. The ratio $\sigma_{\mathit{eff}}(\bar{\theta})/\sigma_2$ only depends on the geometries of Ω_1 and Ω.

In this section we first present results for square tessellations, i.e. when the domain Ω is the unit square. Those results have been obtained using an implementation of Algorithm 1 in the finite element software Freefem (Hecht, 2012). With the expressions (26) and (27) for the constitutive energy-density functions, the boundary value problem (2) becomes

$$\begin{aligned} &\operatorname{div} \boldsymbol{j} = 0 \text{ in } \Omega_2,\ \boldsymbol{j} = \sigma_2|\bar{\boldsymbol{e}} + \nabla u|^{m-1}(\bar{\boldsymbol{e}} + \nabla u) \text{ in } \Omega_2, \\ &u + \bar{\boldsymbol{e}} \cdot \boldsymbol{x} = c^0 \text{ on } \partial\Omega_1,\ u \text{ periodic}, \boldsymbol{j} \cdot \boldsymbol{n} \text{ anti-periodic} \end{aligned} \tag{29}$$

where c^0 is a constant that can be set to 0 without loss of generality. Regarding the finite element computations, only the domain Ω_2 occupied by material 2 needs

to be meshed. We used a simple implementation of Algorithm 1 in which a new finite-element mesh is created from scratch at each update of the geometry. Some computational time could be saved by using nodes relocation strategies. For $m \neq 1$, the boundary value problem (29) is nonlinear and was solved iteratively using a Newton method. As detailed in Sect. 4, solving (29) allows one to evaluate J and its gradient J'. The projection operator $\mathcal{P}$ was calculated following the results presented in Appendix A. The quartic equation (A.7) characterizing the projection was solved using a bisection method. Typical values for the algorithm parameters were $N_{iter} = 100$ and $\alpha_{min} = 10^{-10}$.

5.1. The linear case

Let us first consider the linear case $m = 1$. In that case, the effective conductive behavior of square symmetric material is necessarily isotropic, i.e. σ_{eff} does not depend on the loading direction $\bar{\theta}$ and therefore $\sigma_{\mathit{eff}}/\sigma_2$ is entirely determined by the inclusion shape Ω_1. In Fig. 3 are shown the inclusion shapes obtained by applying the presented procedure with $M = 7$ and $\bar{\theta} = 0$. The average running time for solving problem (24) was about 10 s (on a workstation equipped with an Intel i7-8700@3.2 GHz CPU). Meshes with about 10000 linear triangular elements were used in the finite-element computations reported in the following. Using such a relatively high mesh density ensures that the error between the obtained effective conductivities and theoretical bounds is only limited by the parameters $(M, N_{iter}, \alpha_{min})$ of the shape minimization algorithm and not by the mesh used for the finite element calculations.

From (16), optimal inclusions are characterized by the constancy of $[\![w]\!]_{sym}$ on $\partial\Omega_1$. In Fig. 4 is shown the computed distribution of $[\![w]\!]_{sym}$ on $\partial\Omega$, as obtained from the shape optimization algorithm in the case $c_1 = 0.5$. The plots in Fig. 4 shows the value of $[\![w]\!]_{sym}$ (normalized with respect to $\sigma_2\|\bar{\boldsymbol{e}}\|^2$) as a function of the

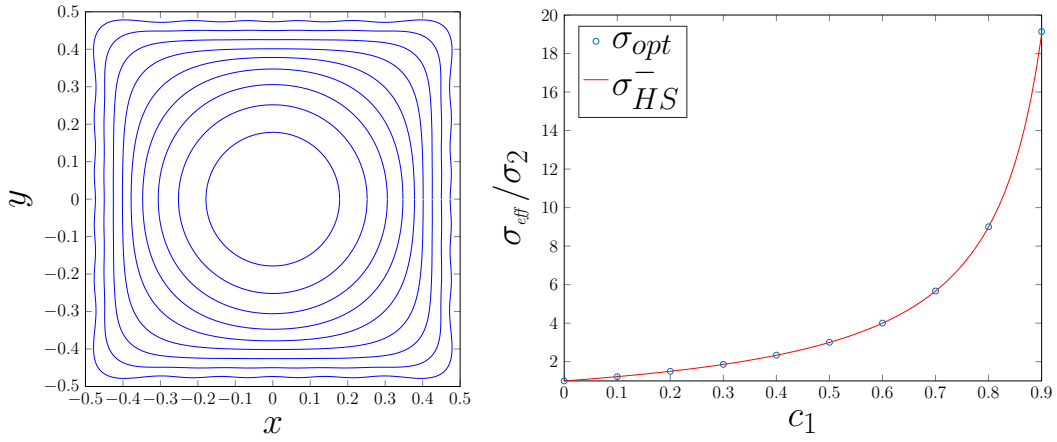

Figure 3: Optimal microstructures for $m = 1$ and $c_1 = i/10$ with $i = 1, \cdots, 9$. Square tessellation.

angular position θ on $\partial\Omega_1$. Because of periodicity, only the values for $0 \leq \theta \leq \pi/2$ are represented. The computed distribution of $[\![w]\!]_{sym}$ satisfies the constancy condition (16) to a good approximation, varying between 3.88 and 4.04 with a mean value of 3.97 and a standard deviation of 0.05. As a comparison, the distribution of $[\![w]\!]_{sym}$ for a circular inclusion varies between 2.45 and 7.14 with a mean value of 4.51 and a standard deviation of 1.66.

The inclusion shapes in Fig. 3 actually correspond to some of the microstructures obtained by Vigdergauz (1994) for the related problem of finding the inclusions that optimizes the elastic energy in grained elastic composites. The microstructures found by Vigdergauz (1994) depend on the applied strain $\bar{\boldsymbol{\varepsilon}}$. For a purely hydrostatic strain $\bar{\boldsymbol{\varepsilon}}$, the Vidgergauz microstructure has square symmetry and its effective bulk modulus K_{eff} is equal to the Hashin-Shtrikman lower bound K^-_{HS} (Hashin and Shtrikman, 1963). As detailed in Appendix B, the cross-properties bounds of Gibiansky and Torquato (1995) imply that the effective conductivity of that microstructure is necessarily equal to the Hashin-Shtrikman lower bound σ^-_{HS} on the effective conductivity, given by $\sigma^-_{HS} = \sigma_2(1 + c_1)/(1 - c_1)$. Those results are recovered from the

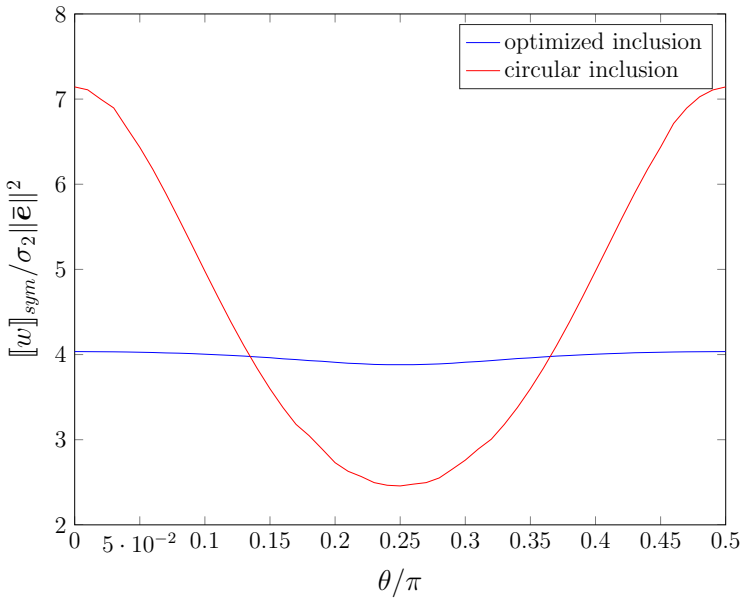

Figure 4: Distribution of $[\![w]\!]_{sym}$ on the boundary of the inclusion. Square tessellation.

present calculations: the effective conductivity σ_{opt} of the optimized microstructures shown in Fig. 3 is indeed very close to the Hashin-Shtrikman lower bound σ^-_{HS}, with a relative error $\sigma_{opt}/\sigma^-_{HS} - 1$ that does not exceed 0.25% for $c_1 \leq 0.9$ and 0.03% for $c_1 \leq 0.8$ (Fig. 5). That relative error is notably due to the truncation of the Fourier expansions to a finite order M in (22). To investigate that point in more detail, the optimization problem (24) has been solved for several values of M. The relative error $\sigma_{opt}/\sigma^-_{HS} - 1$ is shown in Fig. 5 as a function of the volume fraction c_1. For high value of c_1, the relative error tends to increase steeply because the optimal inclusion become more square-like and requires more Fourier coefficients to be approximated accurately. For any given volume fraction c_1, the relative error decreases as M increases and is expected to converge to 0 as $M \to \infty$. Note that taking $M = 5$ is enough for ensuring that the relative error remains below 1% for volume fractions c_1 up to 0.9 (and below 0.04% for $c_1 \leq 0.8$). We keep the value $M = 5$ for all the

examples presented next in this Section. For $c_1 \leq 0.6$ we can observe on Fig. 5 that the error does not get better with higher M. This is a numerical artefact due the values (N_{iter}, α_{min}) used for the convergence criterion in Algorithm 1. For $c_1 \leq 0.6$, the differences between the effective conductivities obtained from different values of M are actually very small and require more stringent values of (N_{iter}, α_{min}) to be captured.

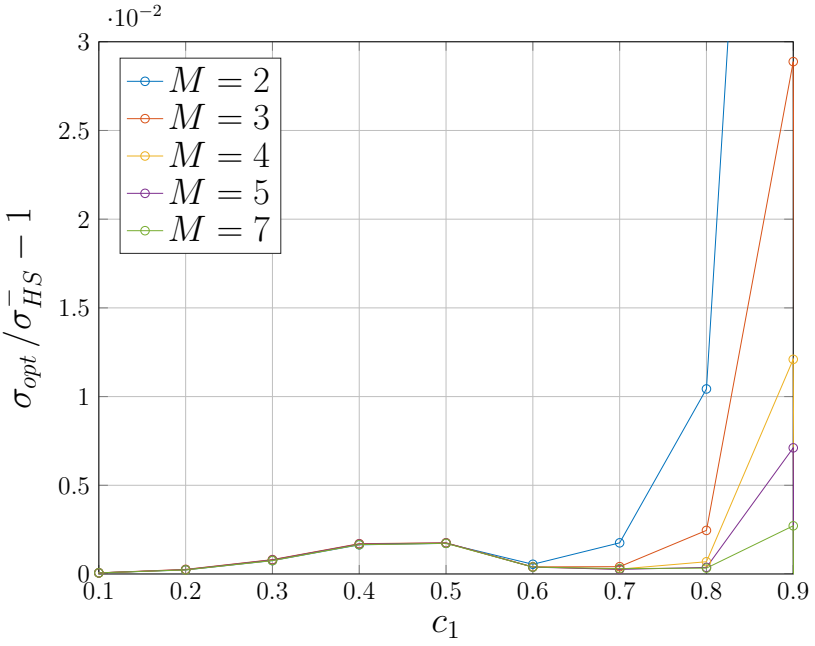

Figure 5: Influence on M on the relative error $\sigma_{opt}/\sigma_{HS}^{-} - 1$ between the effective conductivity σ_{opt} corresponding to the optimized inclusion and the Hashin-Shtrikman lower bound σ_{HS}^{-} in the linear case.

It can be observed that the inclusions in Fig. 3 are symmetric with respect to the x axis, which follows from the symmetry of the problem with respect to that axis. This implies that the coefficients b_k in (22) vanish. The microstructures shown in Fig. 3 are thus determined by the coefficients (a_k) through the polar equation $r = \sum_{0=1}^{M} a_k \cos 4k\theta$. This makes for a very simple representation of those

c_1	a_1	a_2	a_3	a_4	a_5
0.1	0	0	0	0	0
0.2	-0.0005	0	0	0	0
0.3	-0.0032	0	0	0	0
0.4	-0.0096	0.0002	0	0	0
0.5	-0.0220	0.0016	0	0	0
0.6	-0.0400	0.0062	-0.0012	0.0002	0
0.7	-0.0539	0.0118	-0.0034	0.0011	-0.0004
0.8	-0.0649	0.0176	-0.0067	0.0030	-0.0014
0.9	-0.0733	0.0228	-0.0106	0.0060	-0.0038

Table 1: Coefficients defining approximated Vidgergauz inclusions in square tessellations.

microstructures, which could useful notably for manufacturing them. In Table 1 are reported the coefficients $(a_i)_{1\leq 5}$ calculated for $M = 5$. The coefficient a_0 is given by

$$a_0 = \sqrt{\frac{c_1}{\pi} - \frac{1}{2}\sum_{i=1}^{5} a_i^2}.$$

Similar tables are given in (Vigdergauz, 2006) for the truncated Laurent expansion of the conformal map from the unit circle to the optimized inclusion in the context of plane elasticity.

5.2. Influence of the loading direction

For $m \neq 1$, the effective conductivity σ_{eff} in (28) is expected to depend on the loading direction $\bar{\theta}$. In the case of square tessellations, σ_{eff} is a $\frac{\pi}{2}-$periodic function of $\bar{\theta}$ as illustrated in Fig. 6(blue curve) for a circular inclusion with $m = 2$ and $c_1 = 0.3$. As a consequence, the extremal inclusion shape is also expected to depend

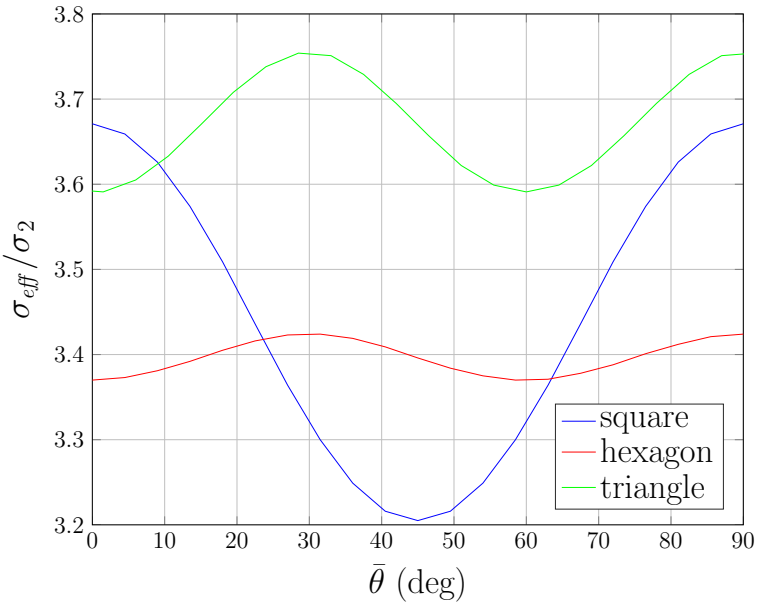

Figure 6: Effective resistivity in the loading direction θ for circular perfectly conducting inclusions in a power-law matrix with nonlinearity index $m = 2$. The volume fraction c_1 of the inclusions is set to 0.3. Three tessellations are considered: square, hexagonal, triangular.

on the loading direction $\bar{\theta}$. This point is illustrated in Fig. 7 showing the optimized inclusion obtained for $\bar{\theta} = 0$ and $\bar{\theta} = \pi/4$. Those loading directions were found to give respectively the highest and the lowest conductivity among all loading directions. The inclusions in Fig. 7 correspond to $c_1 = 0.4$ and $m = 2$. We can observe that the inclusion optimized for $\bar{\theta} = \pi/4$ is less elongated in the $\pi/4$ direction that the inclusion optimized for $\bar{\theta} = 0$. Conversely, the inclusion optimized for $\bar{\theta} = 0$ is less elongated in the $\boldsymbol{u}_x$ direction that the inclusion optimized for $\bar{\theta} = \pi/4$. The average running time for finding the optimized inclusion in the nonlinear case is about 50 s, about 5 times more than in the linear case. The increase in the computation time is mainly due to the Newton iterations needed for solving the boundary value problem (2) in the nonlinear case.

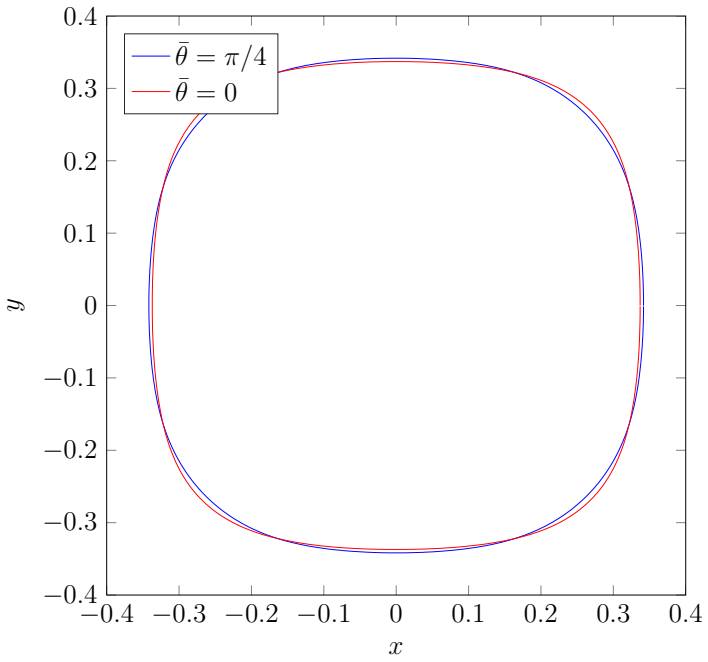

Figure 7: Optimized microstructures for the loading directions $\bar{\theta} = 0$ and $\bar{\theta} = \pi/4$, with $c_1 = 0.4$, $m = 2$.

5.3. Influence of the nonlinearity index

In Fig. 8 are shown the optimized inclusions calculated for $m \in \{2, 5\}$ and $\bar{\theta} = \pi/4$ with several values of the inclusion volume fraction c_1. Taking $\bar{\theta} = \pi/4$ was found to give the minimum effective conductivity. The Vidgergauz microstructures are shown as dotted green lines in Fig. 8. It can be observed that increasing the nonlinearity index m tends to flatten the part $-\pi/4 \leq \theta \leq \pi/4$ of $\partial\Omega_1$, making the inclusion Ω_1 closer to a rounded square. This is especially noticeable for volume fractions c_1 larger than 0.5. Figs. 9 and 10 provide some insight on that phenomenon by showing maps of energy density w_2 as obtained from finite-element simulations with a circular inclusion. Fig. 9(left) corresponds to $c_1 = 0.03$ and $m = 2$. For such a low value of c_1, the energy density map essentially corresponds to the solution of

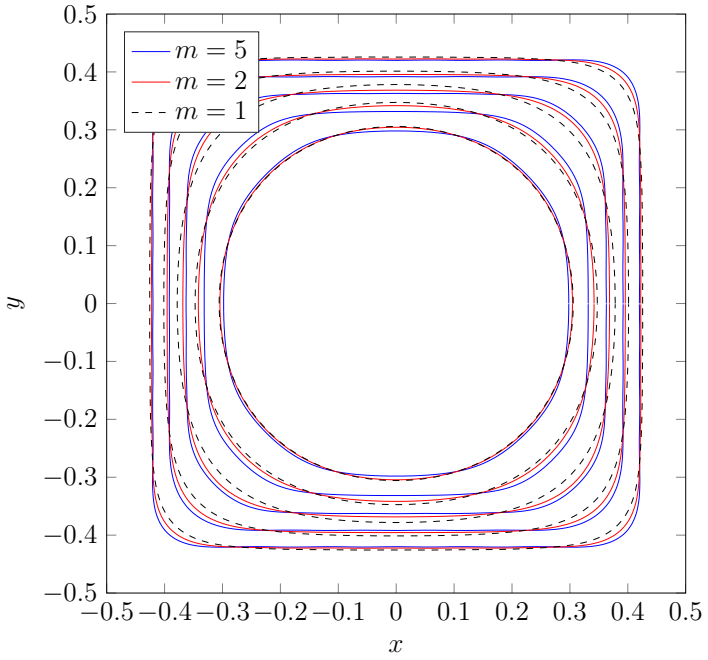

Figure 8: Optimized microstructures for $m = 1, 2, 5$ with $c_1 = i/10$, $3 \leq i \leq 7$.

a single inclusion in an infinite matrix of material 2. In particular, the maximum of w_2 on $\partial\Omega_1$ is reached at $\theta = \pm\pi/4$ (i.e. along the loading direction). As c_1 increases, the interaction between neighboring inclusions comes at play as can be observed in Fig 9(right) showing the energy density map for $c_1 = 0.4$. The energy density is primarily concentrated in the directions $\theta = k\pi/2$ ($k \in \mathbb{Z}$), i.e. around the shortest paths connecting neighboring inclusions. For $c_1 = 0.4$, the maximum of w_2 in reached at the points $\theta = k\pi/2$ on $\partial\Omega_1$. The optimality condition (16) is clearly not satisfied in Fig.9 (right). In the present case we have indeed

$$[\![w]\!]_{sym}(\theta) = \frac{1}{2}\left(w_2(\theta) + w_2(\theta + \frac{\pi}{2})\right)$$

where $w_2(\theta)$ and $[\![w]\!]_{sym}(\theta)$ are respectively the value of w_2 and $[\![w]\!]_{sym}$ at the point of polar angle θ on $\partial\Omega_1$. For $c_1 = 0.4$, the value of $[\![w]\!]_{sym}(0)$ is about $24\sigma_2\|\bar{\boldsymbol{e}}\|^{m+1}$

and largely exceeds the value $[\![w]\!]_{sym}(\pi/4)$ (which is about $10\sigma_2\|\bar{\boldsymbol{e}}\|^{m+1}$). This is an indication that the circular shape is far from optimal in the case $c_1 = 0.4$. Optimizing the shape of the inclusion requires decreasing $[\![w]\!]_{sym}(0)$ and increasing $[\![w]\!]_{sym}(\pi/4)$. This is achieved by increasing the curvature of $\partial\Omega_1$ at $\theta = \pi/4$ and increasing the radius $f(\pi/4)$ of the inclusion in the $\theta = \pi/4$ direction. Increasing the curvature at $\theta = \pi/4$ indeed tends to promote a local energy concentration, in a way similar to stress concentration around sharp corners. This effect is further magnified by increasing $f(\pi/4)$ i.e. reducing the distance between neighboring inclusions in the $\pi/4$ direction. Simultaneously decreasing the curvature $\partial\Omega_1$ at $\theta = 0$ and increasing $f(0)$ has the opposite effect of reducing $[\![w]\!]_{sym}(0)$. Those considerations qualitatively explain the optimized shapes that are found for $c_1 \geq 0.4$ as shown in Fig. 8. In contrast, the variations of $[\![w]\!]_{sym}$ on the boundary remain small in the case $c_1 = 0.04$ depicted in Fig. 9(left), meaning that the circular inclusion is much closer to the optimal shape in that case. When the nonlinearity index m increases, the effects that have been discussed are amplified because the interaction between neighboring inclusions gets stronger. Fig 10(left) illustrates that point by showing the energy density map for a circular inclusion with $m = 5$ and $c = 0.04$. Notice how the energy is less concentrated near the inclusion compared to the case $m = 2$ shown in Fig. 9(left). For $c_1 = 0.4$, the interaction between inclusions is stronger than in the case $m = 2$, resulting in a larger ratio $[\![w]\!]_{sym}(0)/[\![w]\!]_{sym}(\pi/4)$ (which is about 4 in Fig. 10(right) instead of 2.4 in Fig. 9(right)).

As mentioned earlier, the inclusions in Fig. 8 achieve the minimum effective conductivity within the class of microstructures considered. It is interesting to compare their corresponding conductivity σ_{opt} with known Hashin-Shtrikman type bounds on the effective properties of power law composite conductors. Several methods have indeed been proposed to extend the bounds of Hashin and Shtrikman to nonlinear

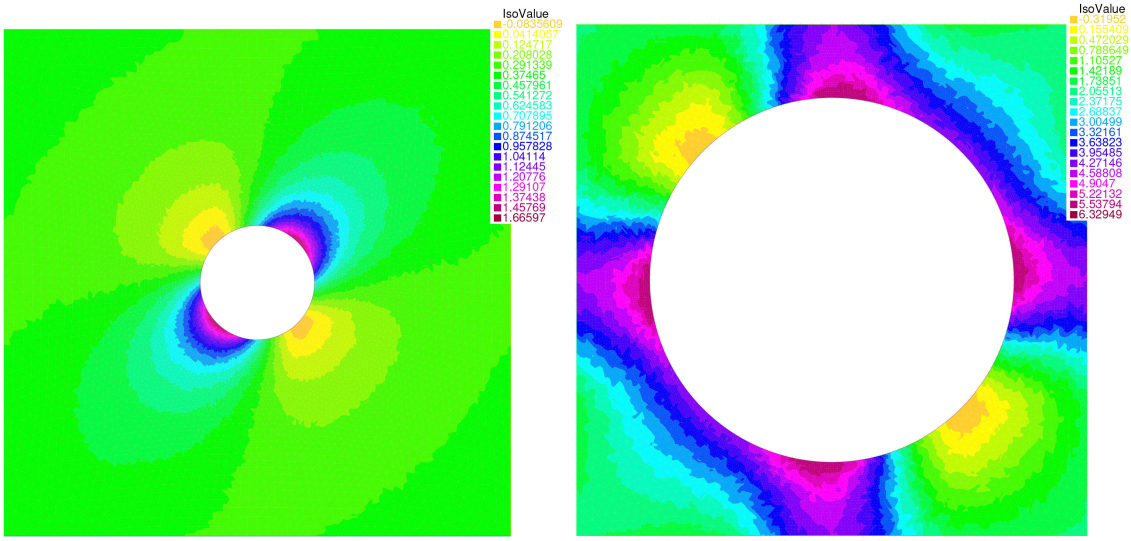

Figure 9: Map of the energy density $w_2/\sigma_2\|\bar{\boldsymbol{e}}\|^{m+1}$ for a circular inclusion in a periodic square cell with $m = 2$. Case $c_1 = 0.04$ (left), $c_1 = 0.4$ (right).

composites. A first method, proposed by Talbot and Willis (1985), makes uses of a homogeneous linear comparison medium and generalizes the variational approach introduced by Hashin and Shtrikman. A second method, due to Ponte Castañeda (1991), employs a heterogeneous linear comparison medium (i.e. a linear comparison composite) having the same microstructure as the original nonlinear composite. Using that last method, any bound on the effective conductivity of the linear comparison composite can be used to generate a corresponding bound for the nonlinear composite. In particular, when the linear Hashin-Shtrikman bound is used, nonlinear Hashin-Shtrikman type bounds are obtained (Ponte Castañeda et al., 1992). For the problem at hand, those two methods give the same Hashin-Shtrikman type lower bound σ_{LC} on the effective conductivity, given by

$$\sigma_{LC} = \sigma_2 \frac{(1+c_1)^{\frac{m+1}{2}}}{(1-c_1)^m}. \tag{30}$$

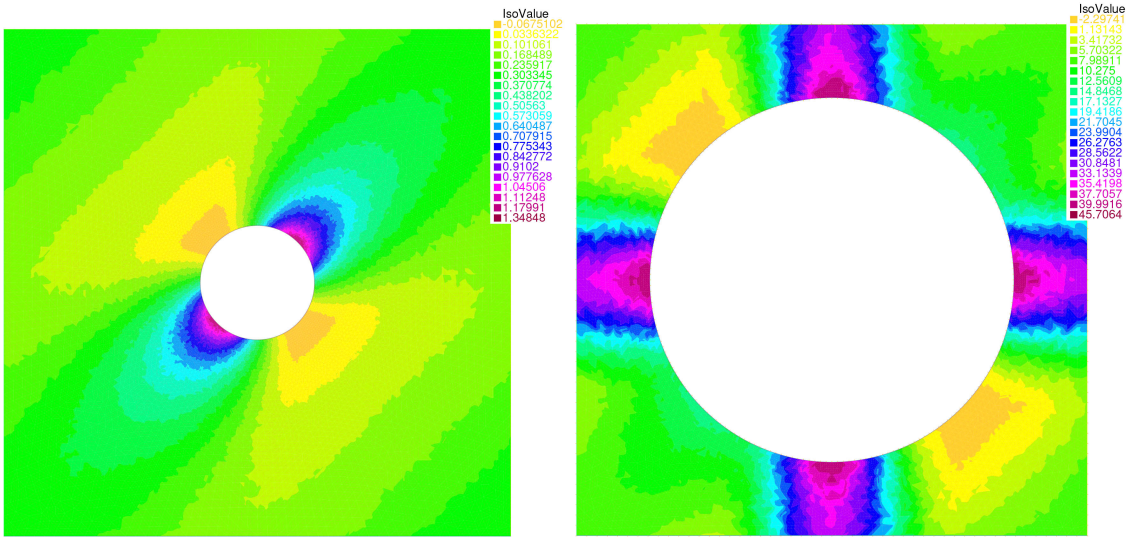

Figure 10: Map of the energy density $w_2/\sigma_2\|\overline{\mathbf{e}}\|^{m+1}$ for a circular inclusion in a periodic square cell with $m = 5$. Case $c_1 = 0.04$ (left), $c_1 = 0.4$ (right).

The subscript LC in σ_{LC} stands for 'Linear Comparison'. The bound σ_{LC} is of the Hashin-Shtrikman type, i.e. it applies to all isotropic composites and is a function of the volume fractions (without any quantitative reference to higher order statistics on the microstructure). For our purpose, it is important to stress that the bound σ_{LC} actually applies to the wider class of composites with square symmetry. As explained by Ponte Castañeda (1992), the bound (30) applies provided that the effective behavior of the linear comparison composite is isotropic, which (in two-dimensional conductivity) is satisfied if the microstructure has square-symmetry (or 3-fold symmetry). For the same reason, the bound σ_{LC} also applies to hexagonal and triangular tessellations that will be considered lated on.

The linear comparison bound is shown in Fig. 11 along with the effective conductivity achieved by the optimized inclusion. The results are shown in terms of the resistivities $\kappa_{opt} = \sigma_{opt}^{-1/m}$ and $\kappa_{LC} = \sigma_{LC}^{-1/m}$. We first observe that $\kappa_{opt} \leq \kappa_{LC}$

i.e. that $\sigma_{LC} \leq \sigma_{opt}$ as expected. In contrast with the linear case, there is a gap between κ_{opt} and κ_{LC}. For any given c_1, the relative difference $(\kappa_{LC} - \kappa_{opt})/\kappa_{LC}$ seems to increase with m. For $m = 2$, $(\kappa_{LC} - \kappa_{opt})/\kappa_{LC}$ reaches a maximum of 2.7% (value attained for $c_1 \simeq 0.3$). For $m = 5$, $(\kappa_{LC} - \kappa_{opt})/\kappa_{LC}$ reaches a maximum of 4.5% (value attained for $c_1 \simeq 0.2$). In terms of conductivity, the relative difference between the effective conductivity of the optimized inclusion and the lower bound σ_{LC} reaches value up to 5.6% for $m = 2$ and up to 25% for $m = 5$. However, it is interesting to observe that κ_{opt} and κ_{LC} almost coincide for large values of c_1, i.e. for small values of c_2. In more detail, note from (30) that $\kappa_{LC}/\kappa_2 = 2^{-(m+1)/2m} c_2$ at the first order in c_2, where $\kappa_2 = \sigma_2^{-1/m}$. The numerical results suggest that

$$\frac{\kappa_{opt}/\kappa_2 - 2^{-(m+1)/2m} c_2}{c_2} \xrightarrow[c_2 \to 0]{} 0$$

i.e. that $\kappa_{opt}/\kappa_2 = 2^{-(m+1)/2m} c_2$ at the first order in c_2, meaning that κ_{opt} and κ_{LC} coincide at the first order in c_2. Consequently, the obtained inclusion shapes give microstructures that (at the first order c_2) are extremal among *all* microstructures with square symmetry. In other words, the effective resistivity of any given microstructure with square symmetry (not necessarily periodic) can only exceed κ_{opt} by a term of the second order in c_2. Those results also indicate that the linear comparison upper bound κ_{LC} in (30) is optimal at the first order in c_2.

6. Hexagonal tessellation

We now consider hexagonal tessellations. In accordance with the 6-fold rotational symmetry of the hexagonal cell, the function $f(\theta)$ is written as

$$f(\theta) = a_0 + \sum_{k=1}^{M} a_k \cos 6k\theta + b_k \sin 6k\theta$$

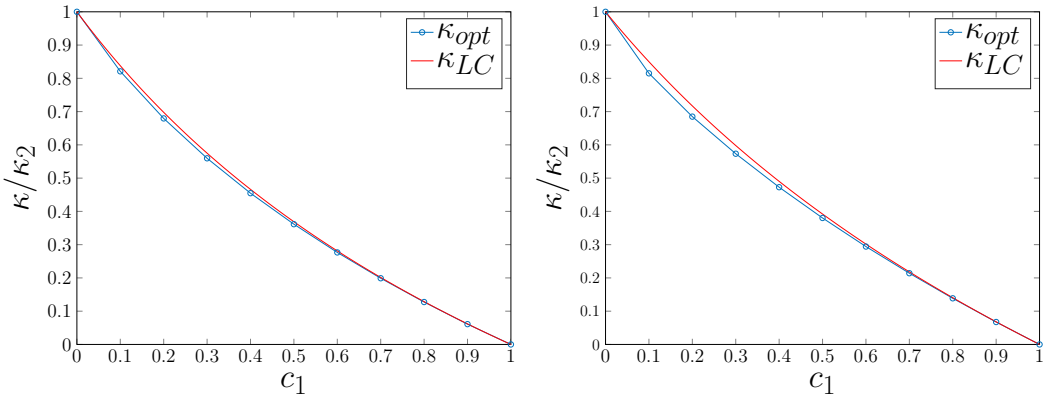

Figure 11: Effective resistivity as a function of the volume fraction c_1, for $m = 2$ (left) and $m = 5$ (right). Square tessellation.

For given values of c_1, m and $\bar{\theta}$, the values of the coefficients (a_k, b_k) that minimize the effective energy are obtained using Algorithm 1.

6.1. Linear case

In Fig. 12 are shown the inclusion shapes obtained numerically for $m = 1$, $\bar{\theta} = 0$, $M = 3$ and for several values of c_1 between 0.1 and 0.9. The effective behavior of a linear material with 6-fold symmetry and isotropic constituents is necessarily isotropic, with regard to both conductivity and elasticity. This is in contrast with square tessellations for which the effective conductivity tensor is isotropic but the effective elasticity tensor is only square-symmetric. The inclusion shapes shown in Fig. 12 correspond to the microstructures derived by Vigdergauz (1999) for finding elastic isotropic materials of extreme bulk modulus when the design domain is a hexagonal periodic cell with a single inclusion. The effective bulk modulus of the microstructures of Vigdergauz (1999) was shown to be equal to the Hashin-Shtrikman bound K^-_{HS}. The cross-properties bounds of Gibiansky and Torquato (1995) imply that the effective conductivity σ_{eff} of those microstructures is equal to the Hashin-

Shtrikman bound σ^-_{HS}. This is indeed what comes out of the numerical simulations. The relative difference $(\sigma_{opt} - \sigma^-_{HS})/\sigma^-_{HS}$ between the Hashin-Shtrikman bound and the calculated effective conductivity σ_{opt} of the microstructures in Fig. 12 indeed remains smaller to 0.25% for inclusion volume fractions c_1 up to 0.9 (and smaller than 0.02% for values c_1 up to 0.8). In the present case, we note that taking $M = 3$ is enough for getting a very good approximation of the optimal inclusion shapes.

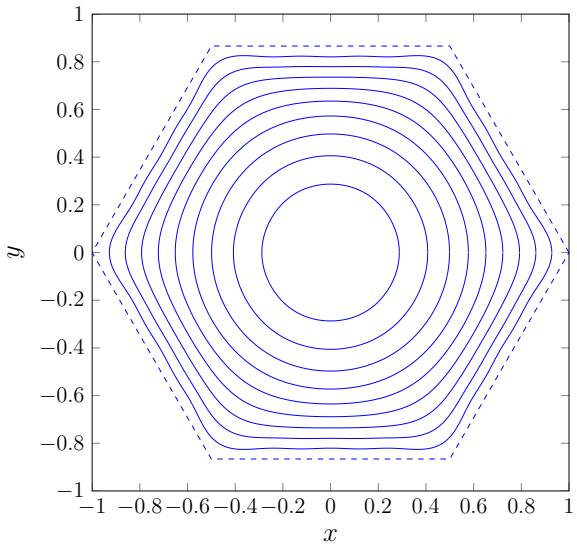

Figure 12: Optimal microstructures for $m = 1$ and $c_1 = i/10$ with $i = 1, \cdots, 9$. Hexagonal tessellation.

In a way similar to the square tessellation considered in Sect. 5, the inclusions are symmetric with respect to the x axis, i.e. the coefficients b_k vanish. The inclusions shown in Fig. 12 are thus entirely determined by the 4 coefficients $(a_0, \cdots, a_3)$ through the polar representation

$$r = a_0 + \sum_{i=1}^{3} \cos 6\pi i\theta$$

c_1	a_1	a_2	a_3
0.1	0.0006	0	0
0.2	0.0008	0	0
0.3	0.0009	0	0
0.4	0.0026	0	0
0.5	0.0081	0.0002	0
0.6	0.0167	0.0012	0.0001
0.7	0.0280	0.0035	0.0006
0.8	0.0389	0.0073	0.0020
0.9	0.0489	0.0123	0.0047

Table 2: Coefficients defining approximated Vidgergauz inclusions in hexagonal tessellations

where

$$a_0 = \sqrt{\frac{3\sqrt{3}c_1}{2\pi} - \frac{1}{2}\sum_{i=1}^{3} a_i^2}.$$

The values of those coefficients $(a_i)_{1\leq 3}$ are reported in Table 2.

6.2. Influence of the nonlinearity index

In the nonlinear case $m \neq 1$, the effective conductivity σ_{eff} of a hexagonal tessellation is no longer isotropic as illustrated in Fig. 6(red curve) showing σ_{eff} as a function of the loading direction $\bar{\theta}$ for a circular inclusion with $m = 2$ and $c_1 = 0.3$. However, observe that the variations of σ_{eff} with $\bar{\theta}$ are much smaller than those corresponding to a square tessellation (blue curve in Fig. 6). This can be attributed to the stronger $6-$fold symmetry of the hexagonal tessellation compared to the 4-fold symmetry of the square tessellation. Also observe in Fig. 6 that the minimum value of σ_{eff} is attained for $\bar{\theta} = 0$. In Fig. 13 are plotted the inclusion shapes obtained by

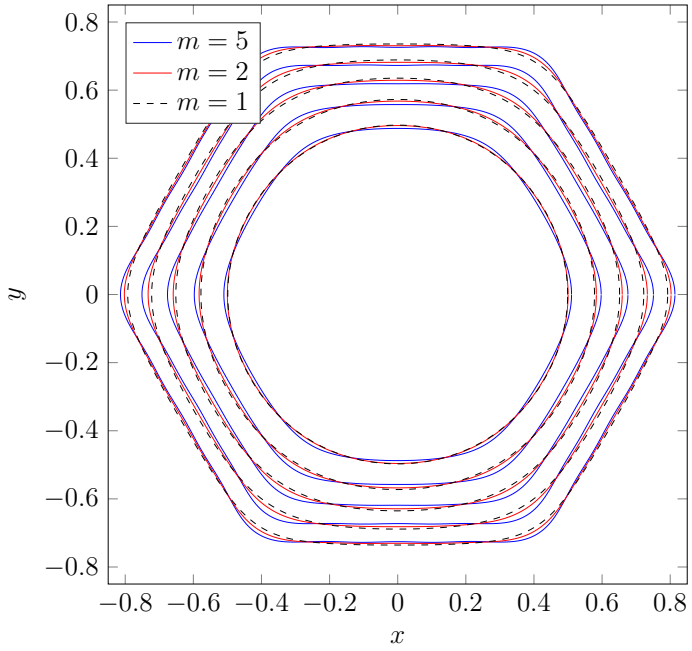

Figure 13: Optimized microstructures for $m = 1, 2, 5$ with $c_1 = i/10$, $3 \leq i \leq 7$. Hexagonal tessellation.

solving (24) for $m \in \{2, 5\}$ and $\bar{\theta} = 0$ with for several values of c_1. For a given c_1, the part $0 \leq \theta \leq \pi/3$ of boundary of the optimized inclusion tends to flatten as m increases. Simultaneously, the radius $f(0)$ of the inclusion increases while the radius $f(\pi/6)$ decreases. This behavior can be interpreted using similar arguments as those presented in Sect. 5.3. In that regard, the energy density map for a circular inclusion with $c_1 = 0.4$ and $m = 2$ is shown in Fig. 14(left). The energy is concentrated in domains connecting neighboring inclusions that are best aligned with the loading direction. The values of energy density shown in Fig. 14(left) can be used to calculated the symmetrized energy density $w_{2,sym}$ and check whether the optimality condition (16) is satisfied by the circular inclusion. The symmetrized energy $w_{2,sym}$, shown in Fig. 14(right), is found to be not constant on the boundary of the circular inclusion.

The ratio $w_{2,sym}(\theta = \pi/6)/w_{2,sym}(\theta = 0)$ is about 1.6, which from (16) shows that the circular inclusion is not optimal. In Fig. 15(left) is shown the energy density map for the optimized inclusion obtained for $c_1 = 0.4$ and $m = 2$. Compared to Fig. 14(left), the value of w_2 at $\theta = 0$ on the boundary of the inclusion is increased, while that value of w_2 at $\theta = \pi/6$ is decreased. The corresponding symmetrized energy density $w_{2,sym}$ is shown in Fig. 15(right). In accordance with the optimality condition (16), the numerical value of $w_{2,sym}$ is close to a constant on $\partial\Omega_1$.

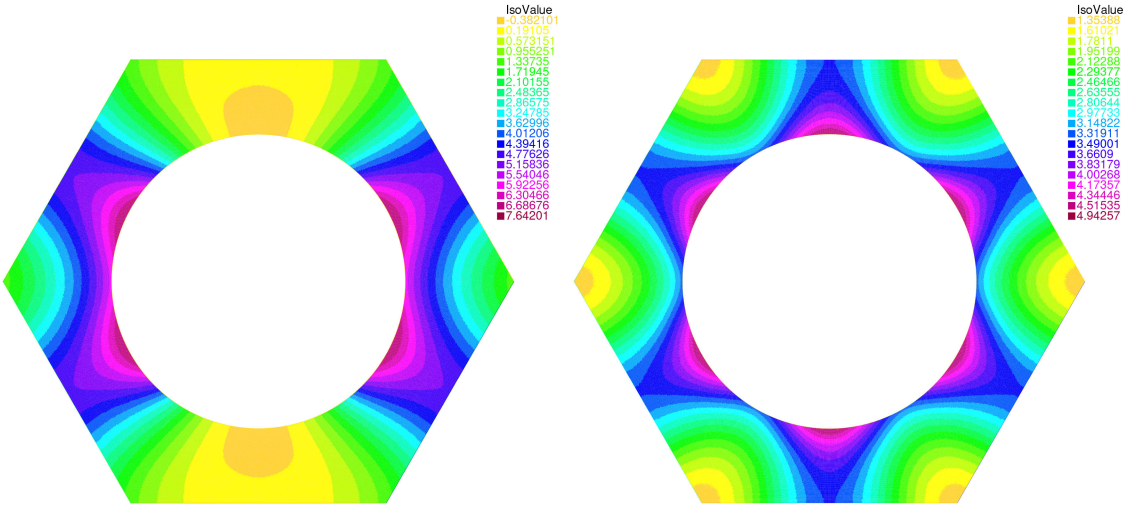

Figure 14: Maps of the energy density $w_2/\sigma_2\|\bar{\boldsymbol{e}}\|^{m+1}$ (left) and symmetrized energy density $w_{2,sym}/\sigma_2\|\bar{\boldsymbol{e}}\|^{m+1}$ (right) for a circular inclusion in a periodic hexagonal cell with $m = 2$, $c_1 = 0.4$, $\theta = 0$.

The effective resistivity $\kappa_{opt} = \sigma_{opt}^{-1/m}$ of the optimized inclusion is shown as a function of c_1 in Fig. 16 and Fig. 17, corresponding to $m = 2$ and $m = 5$ respectively. Let us compare the values κ_{opt} obtained with relevant bounds. The linear comparison bound $\kappa_{LC} = \sigma_{LC}^{-1/m}$ in (30) still applies for material with 6−fold symmetry and is represented as a dotted line in Figs 16 and 17. For any given c_1

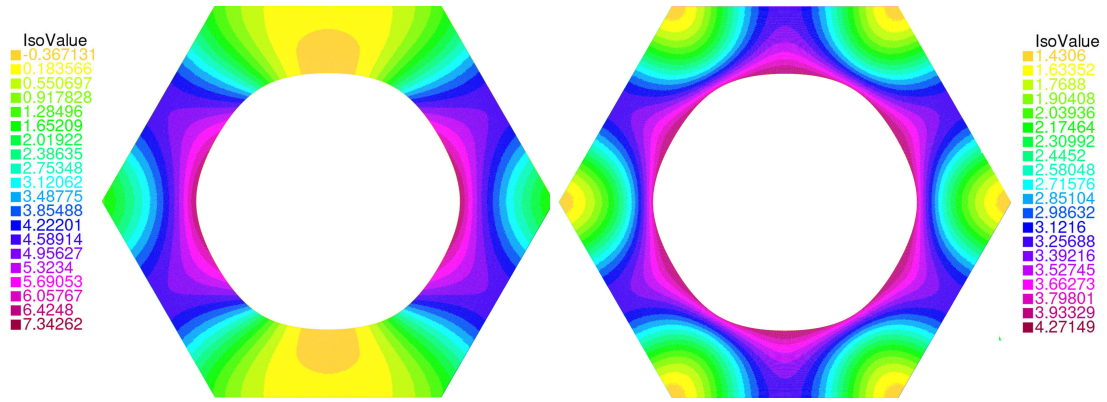

Figure 15: Maps of the energy density $w_2/\sigma_2\|\bar{\boldsymbol{e}}\|^{m+1}$ (left) and symmetrized energy density$w_{2,sym}/\sigma_2\|\bar{\boldsymbol{e}}\|^{m+1}$ (right) for the optimized inclusion in a periodic hexagonal cell with $m = 2$, $c_1 = 0.4$, $\theta = 0$.

and m, the gap $\kappa_{LC} - \kappa_{opt}$ is found to be larger than what is obtained for square tessellations. For $m = 2$, the gap $\kappa_{LC} - \kappa_{opt}$ is maximum for $c_1 \simeq 3$ and reaches $0.03\kappa_2$, which corresponds to a relative difference $(\kappa_{LC}-\kappa_{opt})/\kappa_{LC}$ of approximatively 5%. For $m = 5$, the gap $\kappa_{LC} - \kappa_{opt}$ is maximum for $c_1 \simeq 3$ and reaches $0.056\kappa_2$, which corresponds to a relative difference $(\kappa_{LC} - \kappa_{opt})/\kappa_{LC}$ of approximatively 9%. A tighter Hashin-Shtrikman type bound than the linear comparison bound κ_{LC} has been proposed by Peigney and Peigney (2017) using the translation method (Milton, 2002; Kohn, 1991; Peigney, 2016). That bound –henceforth denoted by κ_T – applies to conductors with 3−fold symmetry, of which hexagonal tessellations are a special case. The bound κ_T is represented as a red solid line in Figs 16 and 17 . For $m = 2$, the gap $\kappa_T - \kappa_{opt}$ reaches a maximum of approximatively $0.01\kappa_2$ (value obtained for $c_1 = 0.4$), which corresponds to a relative difference $(\kappa_T-\kappa_{opt})/\kappa_T$ of approximatively 2%. For $m = 5$, the gap $\kappa_T - \kappa_{opt}$ reaches a maximum of approximatively $0.015\kappa_2$ (value obtained for $c_1 = 0.4$), which corresponds to a relative difference $(\kappa_T-\kappa_{opt})/\kappa_T$

of approximatively 3%. Figs. 16(right) and 17 (right) show a close up of the results near $c_1 = 1$. The plots in Figs. 16(right) and 17 (right) suggest that κ_T and κ_{opt} do not coincide at the first order in c_2. Contrary to the bound κ_{LC}, we note that the bound κ_T cannot be calculated analytically and can only be evaluated numerically. It is possible, however, to derive the first order expansion of κ_T in closed form. The result is

$$\kappa_T = \kappa_2 \frac{c_2}{3}(1 + 2^{-\frac{1}{m}}) + o(c_2).$$

A numerical check shows that κ_{opt}/c_2 does not converge towards $\kappa_2 \frac{1}{3}(1 + 2^{-\frac{1}{m}})$ as c_2 tends to 0, thus confirming that κ_T and κ_{opt} do not coincide at the first order in c_2.

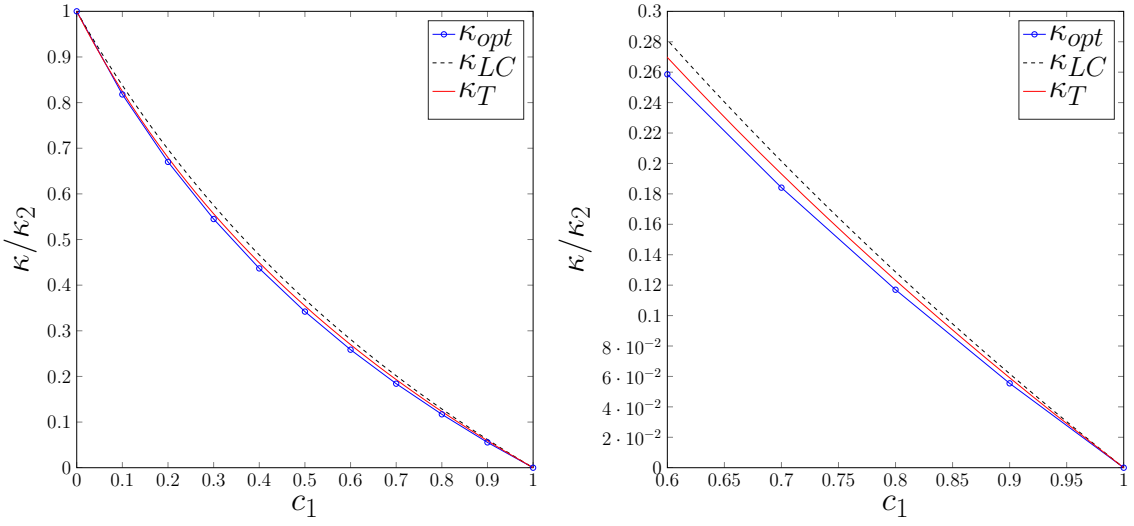

Figure 16: Effective resistivity as a function of the volume fraction c_1 for $m = 2$. Hexagonal tessellation.

7. Triangular tessellations

For triangular tessellations, the periodic cell Ω is formed by 2 neighboring triangles that can be chosen as in Fig. 18. Let O^+ (resp. O^-) be the center of the

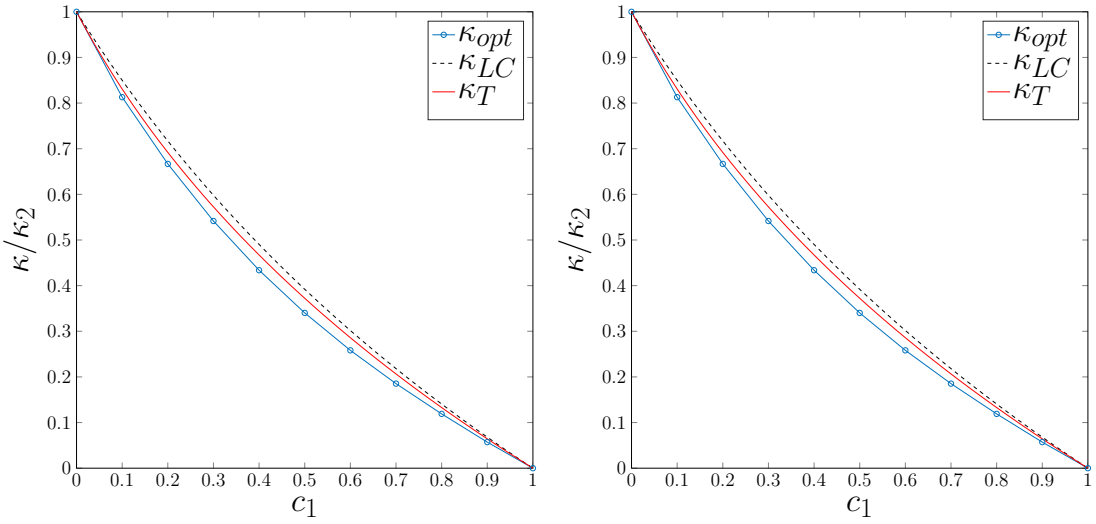

Figure 17: Effective resistivity as a function of the volume fraction c_1 for $m = 5$. Hexagonal tessellation.

right (resp. left) triangle in Ω. In polar coordinates centered at O^+, the boundary of the right inclusion Ω_1^+ is defined by the equation $r = f(\theta)$. In polar coordinates centered at O^-, the boundary of the left inclusion Ω_1^- is defined by the equation $r = f(\theta + \pi)$. In accordance with the 3−fold rotational symmetry of the triangular cell, the function f describing the shape of the inclusion is taken as

$$f(\theta) = a_0 + \sum_{k=1}^{M} a_k \cos 3k\theta + b_k \sin 3k\theta. \tag{31}$$

A slight modification is needed in Algorithm 1 regarding the expressions of the partial derivatives $\frac{\partial J}{\partial a_k}$ and $\frac{\partial J}{\partial b_k}$. The latter have indeed to be updated to account for the fact that the domain Ω now contains 2 (symmetry related) inclusions. Adapting the calculations presented in Sect. 3 shows that

$$\frac{\partial J}{\partial a_k} = \frac{1}{|\Omega|} \int_0^{2\pi} (\llbracket w_+ \rrbracket + \llbracket w_- \rrbracket) f(\theta) \cos nk\theta d\theta$$
$$\frac{\partial J}{\partial b_k} = \frac{1}{|\Omega|} \int_0^{2\pi} (\llbracket w_+ \rrbracket + \llbracket w_- \rrbracket) f(\theta) \sin nk\theta d\theta.$$

where $[\![w_+]\!]$ is the value of $w_2 - w_1$ at the point of polar angle θ on $\partial\Omega_1^+$. Similarly, $[\![w_-]\!]$ is the value of $w_2 - w_1$ at the point of polar angle θ on $\partial\Omega_1^-$.

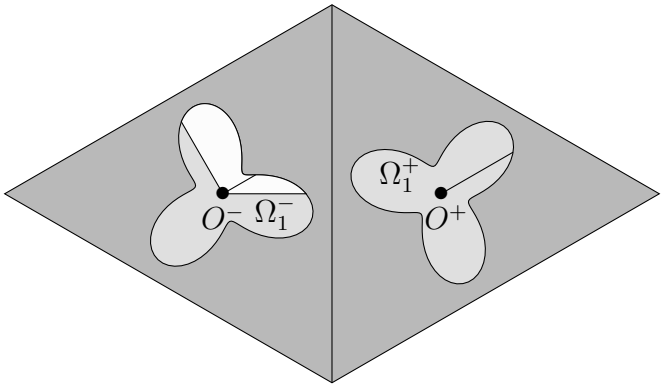

Figure 18: Periodic cell for the triangular tessellation. The two inclusions are symmetry related and have 3-fold symmetry. Degrees of freedom thus correspond to one third of a inclusion (shown in white).

7.1. Linear case

As for the square and the hexagonal tessellations, considering the linear case $m = 1$ allows one to recover known results on the optimal inclusions and to calibrate the number M of needed coefficients. In Fig. 19 are shown the inclusion shapes obtained by running Algorithm 1 with $c_1 = i/10$ ($i = 1, \cdots, 9$). These inclusions shapes correspond to the microstructures obtained by Vigdergauz (1999) for triangular tessellations. The effective conductivity of those microstructures is equal to the Hashin-Shtrikman lower bound σ_{HS}^-. The inclusion shapes in Fig. 19 have been obtained using the value $M = 7$, which was found to be the minimum value ensuring that the relative error between the optimized effective conductivity σ_{opt} and the bound σ_{HS}^- remains below 1% for c_1 up to 0.9 (and below 0.1% for c_1 up to 0.8). The value $M = 7$ is larger than the value $M = 3$ used with the hexagonal tessellation

for reaching the same accuracy in the linear case. This can be attributed to the fact that the optimal inclusions in the triangular tessellation are expected to have sharper corners than the optimal inclusions in the hexagonal tessellation (especially at high value of c_1). A similar argument explains why the value $M = 5$ found for square tessellations falls in between the values of M used for triangular tessellations and hexagonal tessellations. In Table 3 are reported the coefficients $(a_i)_{1\leq 7}$ giving approximations of Vidgergauz inclusions in triangular tessellations, for several values of the inclusion volume fraction c_1. Those approximations are defined by the polar equation

$$r = a_0 + \sum_{i=1}^{7} \cos 3\pi i\theta$$

where

$$a_0 = \sqrt{\frac{\sqrt{3}c_1}{4\pi} - \frac{1}{2}\sum_{i=1}^{7} a_i^2}.$$

7.2. Nonlinear case

In Fig. 6 (green line) is shown the effective conductivity σ_{eff} as a function of the loading direction $\bar{\theta}$ for circular inclusions with $c_1 = 0.3$ and $m = 2$ in a triangular tessellation. Note that σ_{eff} is a $\pi/3$-periodic function of $\bar{\theta}$. The relative variation of σ_{eff} with $\bar{\theta}$ are of the same order as what is obtained for hexagonal tessellation (i.e. about 3%). Also observe in Fig. 6 (green line) that the minimum value of σ_{eff} is attained for $\bar{\theta} = 0$ (modulo $\pi/3$) as for the hexagonal tessellation.

In Fig. 20 are shown the optimized inclusions obtained for $\bar{\theta} = 0$, $m \in \{2, 5\}$ and $c_1 = i/10$ $(i = 3, \cdots, 7)$. The value $M = 7$ has been used in the numerical calculations. Triangular tessellation is the case where the largest difference between the optimized linear inclusion Ω_1^{lin} and the optimized nonlinear inclusion Ω_1^{nlin} is

c_1	a_1	a_2	a_3	a_4	a_5	a_6	a_7
0.1	-0.0002	0	0	0	0	0	0
0.2	-0.0073	0.0003	0	0	0	0	0
0.3	-0.0190	0.0016	0	0	0	0	0
0.4	-0.0330	0.0046	-0.0007	0	0	0	0
0.5	-0.0504	0.0107	-0.0025	0.0005	0	0	0
0.6	-0.0640	0.0171	-0.0054	0.0017	-0.0005	0	0
0.7	-0.0768	0.0247	-0.0100	0.0044	-0.0020	0.0008	-0.0003
0.8	-0.0868	0.0311	-0.0146	0.0078	-0.0045	0.0026	-0.0014
0.9	-0.0937	0.0349	-0.0175	0.0102	-0.0065	0.0044	-0.0029

Table 3: Coefficients for approximated Vidgergauz inclusions in triangular tessellations.

observed. That difference can be measured by the ratio $|\Delta\Omega_1|/|\Omega_1|$ where $\Delta\Omega_1$ is the symmetric difference between the sets Ω_1^{lin} and Ω_1^{nlin}, i.e. $\Delta\Omega_1 = (\Omega_1^{lin} \cup \Omega_1^{nlin}) - (\Omega_1^{lin} \cap \Omega_1^{nlin})$. For triangular tessellation, $|\Delta\Omega_1|/|\Omega_1|$ reaches 14% for $c_1 = 0.4$, $m = 5$. In contrast, for the same values of c_1 and m, $|\Delta\Omega_1|/|\Omega_1|$ is approximatively equal to 6% for square tessellations and equal to 4% for hexagonal tessellations.

The effective resistivity κ_{opt} is reported in Fig. 21. For any given volume fraction c_1, the numerical results show that the resistivity κ_{opt} of the optimized triangular tessellation is always larger than the resistivity of the optimized hexagonal tessellation. Consequently, the gap between κ_{opt} and the upper bound κ_T is reduced and actually becomes relatively small, especially in the case $m = 2$ where $\kappa_T - \kappa_{opt}$ remains smaller than $0.0086\kappa_2$ (value attained for $c_1 \simeq 0.2$) which corresponds to a relative difference of 1.27%. For $m = 5$, the gap between κ_{opt} and κ_T is more noticeable, see Fig. 21. In that case, the maximum gap is $0.268\kappa_2$ (value attained for $c_1 \simeq 0.1$)

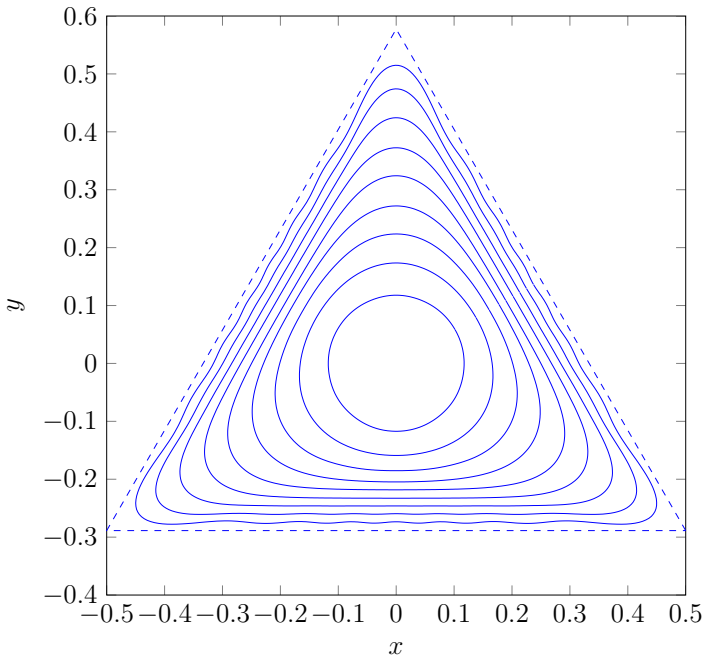

Figure 19: Optimal microstructures for $m = 1$ and $c_1 = i/10$ with $i = 1, \cdots, 9$. The boundary of the triangular cell is shown as a dashed line.

which corresponds to a relative difference of 3.2%. It can be observed in Fig. 21 that κ_{opt} and κ_T seem to coincide at the first order in c_2. The numerical results suggest indeed that

$$\frac{\kappa_{opt}/\kappa_2 - \frac{c_2}{3}(1 + 2^{-\frac{1}{m}})}{c_2} \xrightarrow[c_2 \to 0]{} 0.$$

This indicates that the bound κ_T is optimal at the first order in c_2. Regarding the optimality of the bounds, the triangular tessellation here plays the same role as the square tessellation for the linear comparison bound.

8. Concluding remarks

In linear conductivity, the three types of Vidgergauz microstructures have the same effective conductivity. In contrast, their extension to nonlinear conductivity

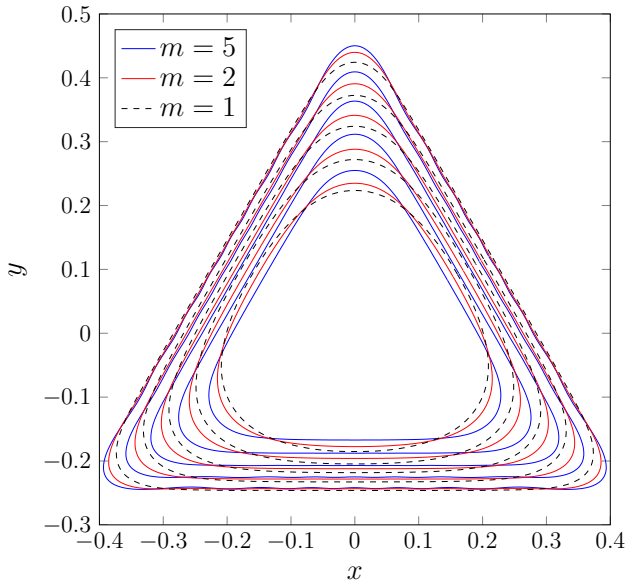

Figure 20: Optimized microstructures for $m = 1, 2, 5$ with $c_1 = i/10$, $3 \leq i \leq 7$. Triangular tessellation.

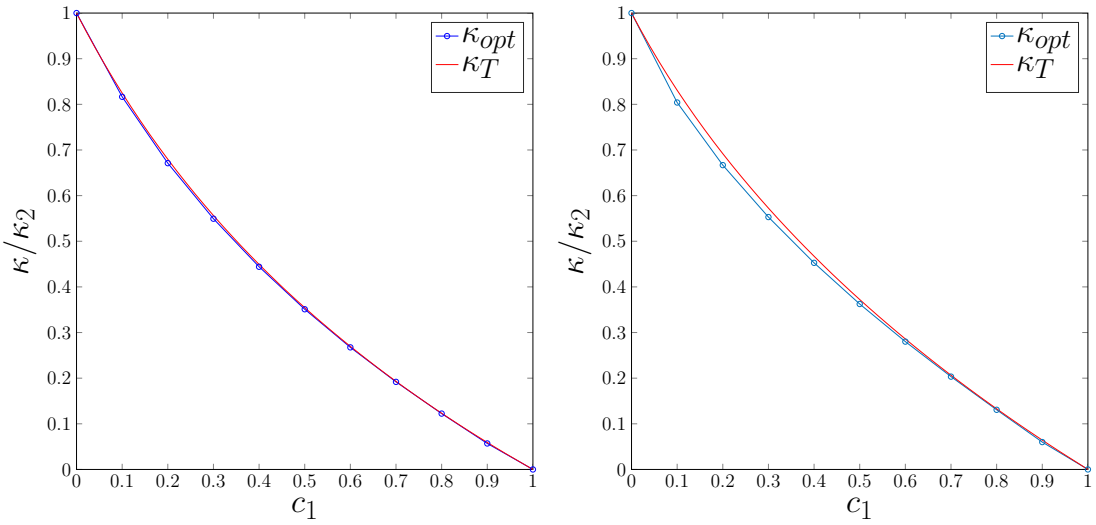

Figure 21: Effective resistivity as a function of the volume fraction c_1 for $m = 2$ (left) and $m = 5$ (right). Triangular tessellation.

all have different effective properties. In particular, the effective behavior of both hexagonal and triangular tessellations show qualitatively similar variations with respect to the loading direction, but the triangular tessellation gives a lower effective conductivity (or, equivalently, an upper effective resistivity). Compared to the linear case, an other distinctive feature of nonlinear extremal inclusions is the fact that they depend on much more parameters. For isotropic power law materials with the same nonlinearity index m_1, the extremal inclusion indeed depends on the conductivity ratio, the loading direction, the nonlinearity index and the inclusion volume fraction, i.e. 4 parameters instead of only 1 in linear conductivity (the Vidgergauz microstructures are indeed independent of the conductivity ratio). If the constitutive materials are allowed to have different nonlinearity indices m_1 and m_2, then 2 additional parameters need to introduced (namely m_2 and $|\overline{\boldsymbol{e}}|$). Hence there is much larger space of parameters to explore compared to the linear case. The gap that exists between the obtained effective properties and known Hashin-Shtrikman type bounds is an other difference with the linear case. Regarding bounds, the results obtained in this paper suggest that the bounds of Talbot and Willis (1985); Ponte Castañeda et al. (1992); Peigney and Peigney (2017) on the effective resistivity of a power law composite with perfectly conducting inclusions are optimal at the first order in the matrix volume fraction c_2.

Aside from power law behavior, the proposed method could be used with other types of nonlinear behavior. More generally, the proposed method could be extended to other two-dimensional problems. Nonlinear elasticity is especially interesting as various bounds of the Hashin-Shtrikman type have been proposed (Talbot and Willis, 1985; Ponte Castañeda, 1991; Talbot and Willis, 2004; Peigney, 2005; Ponte Castañeda, 2012). When dealing with elasticity instead of conductivity, the displacement $\boldsymbol{u}$ would play the role of the potential u. The only major change in

the proposed method lies in problem (1) which would involve the equilibrium equation. The formal expression (19) of the gradient J' as well the layout of Algorithm 1 would remain unchanged. Since the displacement $\boldsymbol{u}$ has two scalar components, computation costs for nonlinear elasticity are expected to be higher than for nonlinear conductivity.

Finally, we stress that the inclusions considered in this paper are extremal only within the class of regular tessellations with a single (simply connected) inclusion in the basic cell. In lack of additional arguments, there is no guarantee that the obtained microstructures are extremal within the whole class of microstructures with prescribed volume fractions and a given order of rotational symmetry. Hence it would be interesting to study a richer class of microstructures and investigate whether effective properties that are closer to the bounds can be obtained. In the linear case, Liu et al. (2008) have shown that there exist other periodic matrix/inclusion-type microstructures than the Vidgergauz microstructures. Those microstructures take the form of multi-coated inclusions, or multiple disconnected inclusions. The method presented could be useful for studying nonlinear extensions of those microstructures. The proposed method could also be used to study rectangular cells and/or non symmetric inclusions. Beyond matrix / inclusions-type microstructures, it would also been interested to study more complex microstructures using topology optimization methods (Allaire, 2012; Bendsøe and Sigmund, 2013).

Appendix A. Calculation of the projection operator $\mathcal{P}$

For a given $\boldsymbol{X}^0 \in \mathbb{R}^{2M+1}$, we address the calculation of the projection $\boldsymbol{X} = \mathcal{P}(\boldsymbol{X}^0)$ on the ellipsoid $\mathcal{E}(c_1, M)$ as defined in Eqs (23) and (25). We first normalize the

problem by setting

$$\boldsymbol{v} = (v_0, \cdots, v_{2M+1}) = \sqrt{\frac{\pi}{2c_1|\Omega|}}\boldsymbol{X},\ \boldsymbol{u} = (u_0, \cdots, u_{2M+1}) = \sqrt{\frac{\pi}{2c_1|\Omega|}}\boldsymbol{X}^0$$

so that

$$\mathcal{P}(\boldsymbol{X}^0) = \tilde{\mathcal{P}}(\boldsymbol{u})$$

where

$$\tilde{\mathcal{P}}(\boldsymbol{u}) = \underset{\boldsymbol{v}\in\tilde{\mathcal{E}}}{\arg\min}\, \|\boldsymbol{v} - \boldsymbol{u}\|^2. \tag{A.1}$$

In (A.1), $\tilde{\mathcal{E}}$ is the ellipsoid with equation

$$1 = 2v_0^2 + \sum_{i=1}^{2M+1} v_i^2. \tag{A.2}$$

Let $\boldsymbol{v}$ be a solution to (A.1). The local stationarity condition reads as

$$u_0 = (1+2\lambda)v_0,\ u_i = (1+\lambda)v_i\ (i \geq 1) \tag{A.3}$$

for some scalar λ. The next step is to determine λ. In the following we focus on the most general situation where $u_0 \neq 0$. Eq. (A.3) implies

$$v_0 = \frac{u_0}{1+2\lambda} \tag{A.4}$$

with $\lambda \neq 1/2$. It can easily be proved that v_0 and u_0 necessarily have the same sign, which yields $\lambda > -1/2$. This notably implies that the second relation in (A.3) can be rewritten as

$$v_i = \frac{u_i}{1+\lambda} \tag{A.5}$$

where the denominator is guaranteed not to vanish. Using (A.4) and (A.5), the condition that $\boldsymbol{v} \in \tilde{\mathcal{E}}$ translates as

$$g(\lambda) = 0 \tag{A.6}$$

where

$$g(\lambda) = 2\frac{u_0^2}{(1+2\lambda)^2} + \frac{\sum_{i\geq 1} u_i^2}{(1+\lambda)^2} - 1.$$

Observe that (A.6) is a quartic equation in $\lambda = 0$. Direct calculations shows that

$$g'(\lambda) < 0 \text{ for } \lambda > -\frac{1}{2}, \quad g(\lambda) \xrightarrow[\lambda \to -\frac{1}{2}]{} +\infty, \quad g(\lambda) \xrightarrow[\lambda \to +\infty]{} -1$$

It follows that the solution to (A.6) on $[-\frac{1}{2}, +\infty)$ is unique. A practical way to solve (A.6) is to use a bisection method. This requires to know an interval $[\lambda_-, \lambda_+]$ that contains the solution, i.e. such that $g(\lambda_+) \leq 0 \leq g(\lambda_-)$. Observing that $g(0) = 2u_0^2 + \sum_{i\geq 1} u_i^2 - 1$, we can take

$$\lambda_- = -\frac{1}{2}, \lambda_+ = 0 \text{ if } 2u_0^2 + \sum_{i\geq 1} u_i^2 \leq 1.$$

In the case $2u_0^2 + \sum_{i\geq 1} u_i^2 > 1$, we have $g(0) > 0$ hence we can take $\lambda_- = 0$. An upper bound λ_+ can be obtained by observing that

$$g(\lambda) \leq \frac{2u_0^2 + \sum_{i\geq 1} u_i^2}{\lambda^2} - 1$$

for any $\lambda > 0$. It follows that $g(\sqrt{2u_0^2 + \sum_{i\geq 1} u_i^2}) \leq 0$ hence we can take $\lambda_+ = \sqrt{2u_0^2 + \sum_{i\geq 1} u_i^2}$. A possible choice for (λ_-, λ_+) is thus

$$\lambda_- = 0, \lambda_+ = \sqrt{2u_0^2 + \sum_{i\geq 1} u_i^2} \text{ if } 2u_0^2 + \sum_{i\geq 1} u_i^2 > .1$$

In summary we have

$$\tilde{\mathcal{P}}(\boldsymbol{u}) = (\frac{u_0}{1+2\lambda}, \frac{u_1}{1+\lambda}, \cdots, \frac{u_{2M-1}}{1+\lambda})$$

where λ is the unique solution to the equation

$$2\frac{u_0^2}{(1+2\lambda)^2} + \frac{\sum_{i\geq 1} u_i^2}{(1+\lambda)^2} = 1 \tag{A.7}$$

on the interval $[\lambda_-, \lambda_+]$ defined by

$$\begin{aligned} &\lambda_- = -\tfrac{1}{2}, \quad \lambda_+ = 0 && \text{if } 2u_0^2 + \sum_{i\geq 1} u_i^2 \leq 1, \\ &\lambda_- = 0, \qquad \lambda_+ = \sqrt{2u_0^2 + \textstyle\sum_{i\geq 1} u_i^2} && \text{if } 2u_0^2 + \displaystyle\sum_{i\geq 1} u_i^2 > 1. \end{aligned}$$

Remark: In the special situation where $u_0 = 0$, it can be proved that $\tilde{\mathcal{P}}(\boldsymbol{u}) = \boldsymbol{u}/\|\boldsymbol{u}\|$ if $\|\boldsymbol{u}\| > 1/2$. If $\|\boldsymbol{u}\| \leq 1/2$, Eq. (A.1) has 2 solutions given by $v_0 = \pm\sqrt{\frac{1}{2} - 2\|\boldsymbol{u}\|^2}$ and $v_i = 2u_i$ for $i \geq 1$.

Appendix B. Effective conductivity of Vidgergauz microstructures

Consider a two-phase linear composite in two dimensions. The two constitutive materials (labelled as 1 and 2) are assumed to be isotropic. In such case, the constitutive laws of material i are characterized by three scalar parameters, namely the conductivity σ_i, the bulk modulus K_i and the shear modulus μ_i. We suppose that $\sigma_1 \geq \sigma_2$ and $\mu_1 \geq \mu_2$. We further assume that the effective behavior of the composite is square symmetric. In such case, the effective constitutive laws of the composite are characterized by four parameters, namely the effective conductivity σ_{eff}, the effective bulk modulus K_{eff} and two effective shear moduli μ_{eff} and μ'_{eff}. Let

$$\sigma_{HS}^- = c_1\sigma_1 + c_2\sigma_2 - \frac{c_1c_2(\sigma_1-\sigma_2)^2}{c_2\sigma_1 + c_1\sigma_2 + \sigma_2}, \;\; \sigma_{HS}^+ = c_1\sigma_1 + c_2\sigma_2 - \frac{c_1c_2(\sigma_1-\sigma_2)^2}{c_2\sigma_1 + c_1\sigma_2 + \sigma_1}$$

be respectively the lower and the upper Hashin-Shtrikman bound on the effective conductivity (Hashin and Shtrikman, 1962). Similarly, let

$$K_{HS}^- = c_1K_1 + c_2K_2 - \frac{c_1c_2(K_1-K_2)^2}{c_2K_1 + c_1K_2 + \mu_2}, \;\; K_{HS}^+ = c_1K_1 + c_2K_2 - \frac{c_1c_2(K_1-K_2)^2}{c_2K_1 + c_1K_2 + \mu_1}$$

be respectively the lower and the upper Hashin-Shtrikman bound on the effective bulk modulus (Hashin and Shtrikman, 1963). The Voigt lower bound on the effective

bulk modulus is denoted by K_h, i.e.

$$K_h = (\frac{c_1}{K_1} + \frac{c_2}{K_2})^{-1}$$

Gibiansky and Torquato (1995) have shown that the pair (σ_{eff}, K_{eff}) necessarily lies in a certain part Γ of the conductivity–bulk modulus plane. That set Γ is bounded by the outermost pair of the 4 hyperbolas

$$\text{Hyp}[(\sigma_{HS}^-, K_{HS}^-), (\sigma_{HS}^+, K_{HS}^+), (\sigma_1, K_h)], \quad \text{Hyp}[(\sigma_{HS}^-, K_{HS}^-), (\sigma_{HS}^+, K_{HS}^+), (\sigma_2, K_h)]$$
$$\text{Hyp}[(\sigma_{HS}^-, K_{HS}^-), (\sigma_{HS}^+, K_{HS}^+), (\sigma_1, K_1)], \quad \text{Hyp}[(\sigma_{HS}^-, K_{HS}^-), (\sigma_{HS}^+, K_{HS}^+), (\sigma_1, K_2)]$$

where $\text{Hyp}[(x_1, y_1), (x_2, y_2), (x_3, y_3)]$ denotes the hyperbola passing through the points (x_1, y_1), (x_2, y_2) and (x_3, y_3). The set Γ is shown in Fig. B.22 in the case $\sigma_1/\sigma_2 =$

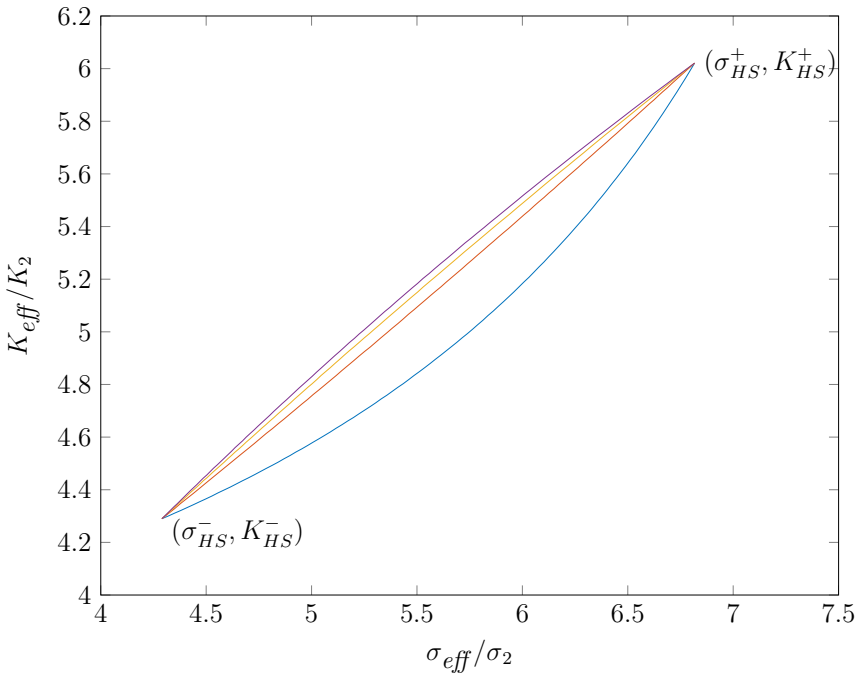

Figure B.22: The set Γ in the case $\sigma_1/\sigma_2 = K_1/K_2 = 20$, $\mu_1/\mu_2 = 10$, $c_1 = 0.4$

$K_1/K_2 = 20$, $\mu_1/\mu_2 = 10$, $c_1 = 0.4$. As illustrated in Fig. B.22, the points

$(\sigma^-_{HS}, K^-_{HS})$ and $(\sigma^+_{HS}, K^+_{HS})$ are corners of the set Γ. More precisely, it can easily be proved that the intersection of Γ with the line $\sigma_{\mathit{eff}} = \sigma^-_{HS}$ reduces to the point $(\sigma^-_{HS}, K^-_{HS})$, i.e.

$$\Gamma \cup \{(\sigma_{\mathit{eff}}, K_{\mathit{eff}}) : K_{\mathit{eff}} = K^-_{HS}\} = (\sigma^-_{HS}, K^-_{HS}) \tag{B.1}$$

Consider now the square-symmetric microstructure of Vigdergauz (1994) with material 1 in the inclusion. In that case, the effective bulk modulus K_{eff} of the Vigdergauz (1994) microstructure is equal to K^-_{HS}. Eq. (B.1) implies that $\sigma_{\mathit{eff}} = \sigma^-_{HS}$, i.e. the effective conductivity of the Vigdergauz (1994) microstructure (with the highest conductive material 1 in the inclusion) is equal to the Hashin-Shtrikman lower bound σ^-_{HS}. The same reasoning applies for the microstructures of Vigdergauz (1999) corresponding to hexagonal and triangular tessellations.

References

Allaire, G., 2012. Shape optimization by the homogenization method. Vol. 146. Springer Science & Business Media.

Bendsøe, M. P., Sigmund, O., 2013. Topology optimization: theory, methods, and applications. Springer Science & Business Media.

Gibiansky, L., Torquato, S., 1995. Rigorous link between the conductivity and elastic moduli of fibre-reinforced composite materials. Philosophical Transactions of the Royal Society of London. Series A: Physical and Engineering Sciences 353 (1702), 243–278.

Grabovsky, Y., Kohn, R., 1995. Microstructures minimizing the energy of a two phase elastic composite in two space dimensions. II: The Vidgergauz microstructure. Journal of the Mechanics and Physics of Solids 43 (6), 949–972.

Hashin, Z., Shtrikman, S., 1962. A variational approach to the theory of the effective magnetic permeability of multiphase materials. J.Appl.Physics. 33 (10), 3125–3131.

Hashin, Z., Shtrikman, S., 1963. A variational approach to the theory of the elastic behaviour of multiphase materials. Journal of the Mechanics and Physics of Solids 11 (2), 127–140.

Hecht, F., 2012. New development in freefem++. J. Numer. Math. 20 (3-4), 251–265. URL `https://freefem.org/`

Kohn, R. V., 1991. The relaxation of a double-well energy. Continuum Mechanics and Thermodynamics 3 (3), 193–236.

Liu, L., James, R., Leo, P., 2008. New extremal inclusions and their applications to two-phase composites. preprint.

Lurie, K., Cherkaev, A., 1984. Exact estimates of conductivity of composites formed by two isotropically conducting media taken in prescribed proportion. Proc. R Soc. Edinburgh A 99 (1-2), 71–87.

Milton, G., 2002. The theory of composites. Cambridge University Press.

Murat, F., Tartar, L., 1985. Calcul des variations et homogénéisation. Les méthodes de l'homogénéisation: théorie et applications en physique 57, 319–369.

Peigney, B., Peigney, M., 2017. Bounds for nonlinear composite conductors via the translation method. Journal of the Mechanics and Physics of Solids 101, 93 – 117.

Peigney, M., 2005. A pattern-based method for bounding the effective response of a nonlinear composite. J. Mech. Phys. Solids 53 (4), 923–948.

Peigney, M., 2016. Improved bounds on the energy-minimizing strains in martensitic polycrystals. Continuum Mechanics and Thermodynamics 28 (4), 923–946.

Ponte Castañeda, P., 1991. The effective mechanical properties of nonlinear isotropic solids. J. Mech. Phys. Solids 39, 45–71.

Ponte Castañeda, P., deBotton, G., Li, G., 1992. Effective properties of nonlinear inhomogeneous dielectrics. Phys. Rev. B 46, 4387–4394.

Ponte Castañeda, P., 1992. New variational principles in plasticity and their application to composite materials. Journal of the Mechanics and Physics of Solids 40 (8), 1757–1788.

Ponte Castañeda, P., 2012. Bounds for nonlinear composites via iterated homogenization. J. Mech. Phys. Solids 60, 1583–1604.

Singer, D. A., 1998. Tiling the plane with regular polygons. In: Geometry: Plane and Fancy. Springer, pp. 21–47.

Talbot, D. R. S., Willis, J. R., 1985. Variational principles for inhomogeneous nonlinear media. IMA Journal of Applied Mathematics 35 (1), 39–54.

Talbot, D. R. S., Willis, J. R., 2004. Bounds for the effective constitutive relation of a nonlinear composite. Proc. R Soc. London A 460 (2049), 2705.

Vigdergauz, S., 1994. Two-dimensional grained composites of extreme rigidity. ASME J. Appl. Mech 61, 390–394.

Vigdergauz, S., 1999. Energy-minimizing inclusions in a planar elastic structure with macroisotropy. Structural optimization 17 (2-3), 104–112.

Vigdergauz, S., 2001. The effective properties of a perforated elastic plate numerical optimization by genetic algorithm. International Journal of Solids and Structures 38 (48-49), 8593–8616.

Vigdergauz, S., 2006. The stress-minimizing hole in an elastic plate under remote shear. Journal of Mechanics of Materials and Structures 1 (2), 387–406.

Vigdergauz, S., 2010. Energy-minimizing openings around a fixed hole in an elastic plate. Journal of Mechanics of Materials and Structures 5 (4), 661–677.